Double Master's Degree Program

Università degli Studi di Padova

Dipartimento di Ingegneria Civile, Edile ed Ambientale

Mathematical Engineering

Mathematical Modelling for Engineering and Science

Universitat Politècnica de Catalunya

Departament d'Enginyeria Civil i Ambiental

Numerical Methods in Engineering

Master Thesis

Development of a topology optimization simulation tool for thermal management systems

Candidate:	Savona Enrico
UniPd Supervisor:	Putti Mario
UniPd Co-Supervisor:	Larese Antonia
UPC Supervisor:	Giacomini Matteo

Academic year 2022/2023

Abstract

Conjugate heat transfer (CHT) problems play a crucial role in the modelling and simulation of cooling phenomena in thermal management systems, e.g., for batteries of electric vehicles. CHT involves the solution of a system of coupled partial differential equations, encompassing the incompressible Navier-Stokes equations for the fluid and the Fourier equation for the thermal phenomena. Topology optimization provides, in turn, a framework to use CHT simulations to derive optimal configurations for heat sinks, maximizing efficiency. This project focuses on the development and implementation of a numerical simulation tool for CHT problems, integrating it in a topology optimization pipeline based on the adjoint. Numerical results are presented to showcase the capability of the method to derive efficient geometries in the context of a multi-objective optimization problem of a fluid-thermal system.

Contents

Chapter 1

Introduction

In recent years, the topic of topology optimization has been gaining significant traction in many branches of industrial design and engineering. The purpose of topology optimization is to find the distribution of materials in a domain that minimizes a given objective functional. According to [1], a topology optimization problem is defined by three elements: a model of the physics, a given quantity to minimize on the domain, (i.e. an objective functional), and a set of optimization variable to model any shape restrictions required. Among the different methods of shape optimization, three main branches can be identified:

- Sizing optimization aims to maximize to objective varying some given parameter defining the shape in question, like thickness or diameter. [2], [3]
- Geometric (shape) optimization allows finding the optimal configuration without imposing initial restrictions on the shape, by moving its boundary. No changes in the configurations are permitted. [4], [5]
- Topology optimization has the highest degrees of freedom between these choices, and it is often associated with more dramatic improvements in the final configuration because of this. It allows changes in the internal topology of the domain, since it does not restrict the shape nor the number of connected regions in the final configuration. [6], [7]

These methods, nowadays have been used in disciplines as varied as aerodynamics [8], acoustic [9] and electromagnetics [10], and topology optimization in particular has been applied with success to structural design [11] and heat transfer [12].

The field was kick-started in the late 1980s by [13] using the homogenization method and, since then, several approaches have been proposed to tackle topology optimization. The most successful can be divided in density-based methods, level set methods, and phase-field methods. Among density methods the most prominent is the Solid Isotropic Material with Penalization (SIMP) method, which employs explicit penalization terms to describe the physics in different media. It is often found in commercial software due to its simplicity, but it is plagued by some problems like dependency on the mesh and the appearance of checkerboard patterns, a phenomenon in which the design variable develops oscillations in the domain. Several techniques have been developed to solve these problems, most prominently filtering methods [14].
The level set method represents the materials on the domain using the zero-level set of a function, that evolves following the Hamilton-Jacobi equation [15]. Its main problems are represented by the need for reinitialization [16], and the limitations on the transformations allowed on the domain, sometimes solved augmenting the method with topological sensitivities, but paying the price of slower convergence [17].
Finally, phase-field methods represent the materials with density-like variables but, contrary to SIMP, employ an implicit penalization. Different approaches ([18], [19]) have been employed to guide the evolution of the algorithm, This method is hampered by a slow convergence rate [20] and the complexity of interpreting the meaning behind the indistinct gray, intermediate region within the domain. Consequently, an appropriate post-process addressing these aspects is needed.

The selection of a strategy for computing design sensitivities, crucial for informing algorithms on simulated physics, represents a method-defining decision. Among the various options, the adjoint method has garnered significant attention from researchers due to its effectiveness across a wide array of problems [15]. Originally developed by Pontryagin for ordinary differential equations [21] and later extended to distributed systems, specifically partial differential equations, by Lions [22], the adjoint method is favored for the relatively modest computational burden it represents in sensitivity analysis. This method involves formulating the Lagrangian of

the problem, which, in turn, yields a set of adjoint equations and associated boundary conditions collectively known as the adjoint problem.

The application of topology optimization to fluid dynamics, and in tandem the optimization of heat sink design stand as an intricate topics attracting increasing research focus. This journey commences with the seminal work of Borrvall and Petersson [23], who introduced a method for fluid-only problems. This method incorporates the definition of a porosity field across the domain, with high values in fluid-filled regions and low values in solid-filled areas. A fictitious force based on Darcy's law is then introduced to penalize the velocity field in solid sections, allowing the treatment of topology optimization problems in flow simulations without the need for distinct meshes or distinct sets of equations. Building on this foundation, subsequent advancements have extended the model applicability. Initially expanded to handle the incompressible Navier-Stokes equation [24–26], the model has progressed to encompass the coupled energy equation as well ([12, 27]). The most successful works in this field have employed the level set method to obtain optimal configurations and test them experimentally [28], [29], but always using a single objective functional [30], [12].

In most real world applications, however, factors other than heat dissipation must be accounted in the design of a heat sink. Most prominently, the pressure drop required to drive the flow through the chamber. In the context of multi-objective topology optimization, the set of optimal non-dominated solutions is called Pareto frontier. Relevant techniques to locally explore the optimization front include, but are not limited to, the weighted sum method [31], the ε-constrained method [32], the normal boundary intersection method [33], and adaptive weighting methods [27].
The problem of optimization for heat sinks is also garnering attention due to its application in the field of electric vehicles. One of the engineering challenges that still lacks a definitive solution is the cooling of the batteries powering these vehicles, whose performance and safety heavily depend on the temperature range they operate in. The current way to design this cooling system is shown in figure 1.1: the batteries are laid upon a metal sheet, pressed mechanically to draw channels that allow and organize the flow of the cooling fluid.

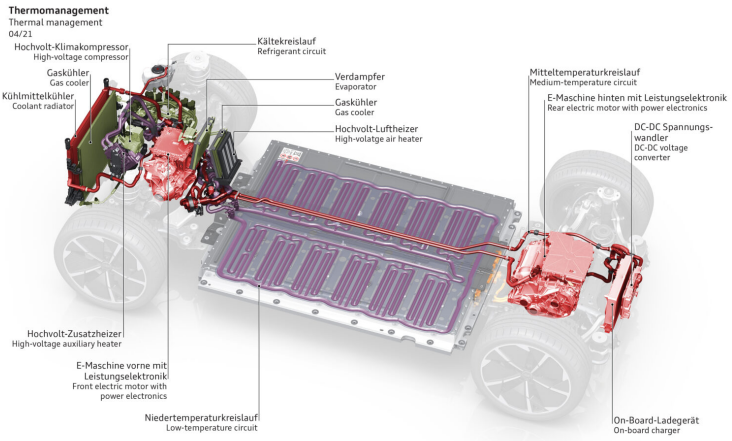

Figure 1.1: Representation of a cooling system for electric vehicles [34]

The classic serpentine structure proves inefficient, since the fluid loses most of its cooling power by the time it reaches half of the duct, and current efforts in topology optimization are directed towards the development of a tool capable of designing optimal structures for this application.

This thesis draws upon a combination of the phase-field and the SIMP method to represent the design domain in a multi-objective problem, treated with the weighted sum method. Based on the approach of [35], the design variable evolves via a Reaction-Diffusion Equation (RDE) [36], aided by a Double Well Potential (DWP) [18]. This approach allows for changes in the internal topology of the domain, controlling the complexity of structures with the diffusion coefficient, while the problem of gray zones is solved in a few iterations of post-process with the DWP. The PDEs that model the physics are solved using the Finite Elements Method (FEM) implemented in an in-house solver. The code is written using the software FreeFem++ [37], a versatile macro of the coding language C++ that automates the discretization of a given weak form, with a high performance yield. The method and its implementation are then applied to the exploration of the Pareto front, and the discussion of the results.

This dissertation is divided into the following parts: in chapter 1 the physical problem and its extension to account for the solid domain is presented, and the optimization problem is stated; chapter 2 is devoted to the presentation of the mathematical model, containing all the computations needed to derive the systems of PDEs and specializing them to the problem at hand. Chapter 3 discusses the numerical implementations of the model presented in the previous chapter, explaining the various choices made along the way and explaining the algorithm in detail. In chapters 4 and 5, after focusing on the validation of the various parts of the solver, the results obtained are presented and discussed. The possible directions for future work are explored in the conclusion.

Chapter 2

Problem Statement

2.1 The Primal Problem

Consider a compact set $\bar{\Omega} = \Omega \cup \partial\Omega$ belonging to $\mathbb{R}^d$ and let $\partial\Omega = \Gamma_N \cup \Gamma_D$ be different parts of the boundary. Suppose that Ω is composed of a portion filled with solid Ω_s, and a portion filled with fluid $\Omega_f = \Omega \backslash \Omega_s$. The incompressible Navier-Stokes equations for a Newtonian fluid can be expressed on Ω_f in dimensionless form as

$$\begin{aligned} (\boldsymbol{u}\cdot\nabla)\boldsymbol{u} - \frac{1}{\mathrm{Re}}\nabla^2\boldsymbol{u} + \nabla p &= \boldsymbol{b} && \text{in } \Omega_f, \\ -\nabla\cdot\boldsymbol{u} &= 0 && \text{in } \Omega_f, \\ \boldsymbol{u} &= \boldsymbol{u}_D && \text{on } \Gamma_D, \\ \frac{1}{\mathrm{Re}}(\boldsymbol{n}\cdot\nabla)\boldsymbol{u} - p\boldsymbol{n} &= \boldsymbol{\tau} && \text{on } \Gamma_N. \end{aligned} \tag{2.1}$$

The first equation is obtained substituting the Cauchy stress using Stokes' law with the regular gradient instead of the symmetric part.

Notice that the Neumann boundary condition is not a boundary traction but a "pseudo-traction". A proper traction should be imposed in terms of the stress tensor:

$$\boldsymbol{n}\cdot\boldsymbol{\sigma} = -p\boldsymbol{n} + 2\frac{1}{\mathrm{Re}}\boldsymbol{n}\cdot\nabla^{\mathrm{s}}\boldsymbol{u} \neq -p\boldsymbol{n} + \frac{1}{\mathrm{Re}}(\boldsymbol{n}\cdot\nabla)\boldsymbol{u}$$

These two formulations are equivalent under appropriate hypotheses. See [38]. Suppose that the corresponding dimensionless energy equation holds, namely,

$$\begin{aligned} \mathrm{Re}\ \mathrm{Pr}\,(\boldsymbol{u}\cdot\nabla)\,T - \Delta T &= 0 && \text{in } \Omega \\ T &= T_D && \text{on } \Gamma_D \\ \boldsymbol{n}\cdot\nabla T &= 0 && \text{on } \Gamma_N \end{aligned} \tag{2.2}$$

The non-dimensional analysis has been carried out with the following definitions

$$\begin{aligned} &\mathrm{Re} = \frac{\rho U L}{\mu}, \quad \mathrm{Pr} = \frac{\mu c_{\mathrm{p}}}{k_s}, \\ &\nabla = L\bar{\nabla}, \quad \mathbf{u} = \frac{\overline{\mathbf{u}}}{U}, \quad p = \frac{\bar{p}}{\rho U^2}, \quad T = \frac{\bar{T} - T_{\mathrm{w}}}{T_{\mathrm{B}} - T_{\mathrm{w}}}, \end{aligned}$$

where ρ is density, U, L are characteristic velocity and length and μ is viscosity. In the definition of Prandtl number Pr, c_{p} is specific heat at constant pressure and k_s thermal conductivity. $\bar{\nabla}, \overline{\mathbf{u}}, \overline{\mathbf{p}}$, and $\bar{T}$ represent the dimensional gradient operator, fluid velocity, pressure, and temperature, respectively. T_{B}, and T_{w} are the bulk mean temperature, and the wall temperature, respectively.

2.2 Phase field method for boundary representation

A topology optimization problem as the one at hand is defined to have part of the domain filled with solid and part filled with fluid. Call $\partial\Omega_s$ the interface between these portions of Ω. There are several ways to tackle this

problem, but in recent years methods allowing for the use of a singular mesh for both domains gained popularity. The focus of this work will be on the phase field method in particular, introducing a function $\phi : \mathbb{R}^2 \to \mathbb{R}$ such that $0 \leq \phi \leq 1$. This function is defined as

$$\begin{cases} \phi = 1 \text{ in } \Omega_s \\ 0 < \phi < 1 \text{ in } \partial\Omega_s \\ \phi = 0 \text{ in } \Omega_f = \Omega \backslash \Omega_s \end{cases} \tag{2.3}$$

With this definition ϕ will act as a "density" of sorts, while allowing for a smooth transition between fluid and solid domain, as shown in figure 2.1.

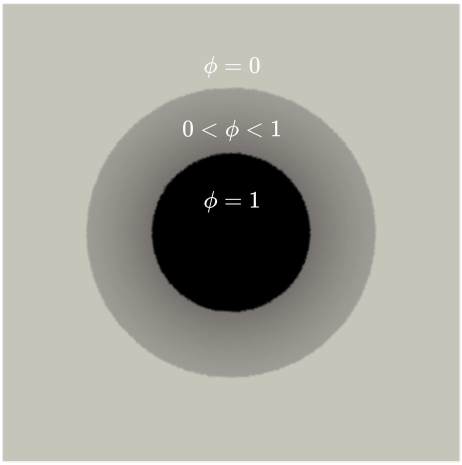

Figure 2.1: Schematic representation of the domain: the algorithm presented allows for a diffuse transition interface between the parts of the domain filled with solid ($\phi = 1$) and those filled with fluid ($\phi = 0$)

2.3 Extension of the state problem to the computational domain

The presence of the solid and its effect on the physics will be modeled using the SIMP method (Solid Isotropic Material with Penalization). A scalar corresponding to the inverse permeability of the medium is defined as $\alpha_{\max} = \frac{1}{\mathrm{Da}}\left(1 + \frac{1}{\mathrm{Re}}\right)$ where $\mathrm{Da} = \frac{L^2}{k}$ is the Darcy number and k is the porosity of the medium. This approach is based on [23]. The SIMP method consists in defining $\alpha_{\min}$ as the permeability on the fluid domain (set to a very low value but not 0 to avoid numerical problems) and finally

$$\alpha(\phi) = \alpha_{\min} + (\alpha_{\max} - \alpha_{\min})\phi^{\zeta}$$

Then the term $-\alpha \boldsymbol{u}$ can be added to the momentum equation, where it acts as a fictitious force penalizing the velocity in the solid. In the parts of the domain where $\phi \sim 1$ (i.e. the solid) the other terms of the momentum equation become negligible and it becomes $\alpha \boldsymbol{u} = \boldsymbol{0}$.

$$(\boldsymbol{u} \cdot \nabla)\boldsymbol{u} - \frac{1}{\mathrm{Re}}\nabla^2 \boldsymbol{u} + \nabla p + \alpha(\phi)\boldsymbol{u} = \boldsymbol{0} \text{ in } \Omega \tag{2.4}$$

A similar approach is adopted to simulate the production of heat inside the solid domain. Using the approach of [30], the production of heat is modeled as $-\Xi(T_{bulk} - \bar{T})$ where Ξ is a coefficient used to artificially regulate the amount of heat produced.
After the adimensionalization this term becomes $-\beta(\phi)(1 - T)$ where $\beta(\phi) = \beta_{\min} + (\beta_{\max} - \beta_{\min})\phi^{\zeta}$ with the SIMP method and $\beta_{\max} = \frac{\Xi L^2}{k_s}$ with k_s being once again the thermal conductivity of the solid.
The resulting extended energy equation is

$$\mathrm{Re}\ \mathrm{Pr}\,(\boldsymbol{u} \cdot \nabla)\, T - \Delta T - \beta(\phi)(1 - T) = 0 \text{ in } \Omega \tag{2.5}$$

The main drawback of using $\beta(\phi)$ to model the generation of heat in the domain, is the incapability to tune it to simulate the characteristics of any specific fluid: its value is, in fact, chosen by similarity to Nusselt number. [12], [27]
For the rest of the discussion call $\alpha := \alpha(\phi)$ and $\beta := \beta(\phi)$, to lighten the notation. From now on the SIMP exponent will be set to $\zeta = 3$, following the most common choice in structural optimization [39].

2.4 Minimization problem

We are interested in minimizing a functional J defined over $\bar{\Omega}$ or part of it, which in general is a function of all the design and primal variables $J := J(\phi, \boldsymbol{u}, p, T)$. As common in topology optimization, a volume constraint is needed, as the problem is ill-posed otherwise. Given a target fraction of the domain to be filled with solid, call $V_0 = \int_\Omega d\Omega$ and $V = \int_\Omega (1-\phi) d\Omega$ such that the full problem can be stated as:

$$
\begin{aligned}
&\min_{\phi} J(\phi, \boldsymbol{u}, p, T) && \text{s.t.} \\
&G = \frac{V}{V_0} - V_{req} < 0 && \\
&\mathbf{R}_{\boldsymbol{u}} = (\boldsymbol{u}\cdot\nabla)\boldsymbol{u} - \frac{1}{\mathrm{Re}}\nabla^2\boldsymbol{u} + \nabla p + \alpha\boldsymbol{u} = \mathbf{0} && \text{in } \Omega, \\
&\mathbf{R}_p = -\nabla\cdot\boldsymbol{u} = 0 && \text{in } \Omega, \\
&\mathbf{R}_T = \mathrm{Re}\ \mathrm{Pr}\,(\boldsymbol{u}\cdot\nabla)\,T - \Delta T - \beta(1-T) = 0 && \text{in } \Omega, \\
&\boldsymbol{u} = \boldsymbol{u}_D && \text{on } \Gamma_D, \\
&\frac{1}{\mathrm{Re}}(\boldsymbol{n}\cdot\nabla)\boldsymbol{u} - p\boldsymbol{n} = \mathbf{0} && \text{on } \Gamma_N \\
&T = T_D && \text{on } \Gamma_D \\
&\boldsymbol{n}\cdot\nabla T = 0 && \text{on } \Gamma_N
\end{aligned}
\tag{2.6}
$$

where $\mathbf{R}_{\boldsymbol{u}}, \mathbf{R}_p, \mathbf{R}_T$ are the residuals of the primal equations in strong form. This is therefore a PDE-constrained optimization problem.

Chapter 3

Continuous adjoint method for topology optimization

3.1 Weak form of the equations

Consider the following spaces:

$$\mathcal{S} := \left\{ \boldsymbol{u} \in \left[\mathcal{H}^1(\Omega)\right]^d \mid \boldsymbol{u} = \boldsymbol{u}_D \text{ on } \Gamma_D \right\} \text{ (trial solutions)} \tag{3.1}$$

$$\mathcal{V} := \mathcal{H}^1_{\Gamma_D}(\Omega) = \left\{ \boldsymbol{w} \in \left[\mathcal{H}^1(\Omega)\right]^d \mid \boldsymbol{w} = \boldsymbol{0} \text{ on } \Gamma_D \right\} \text{ (weighting functions)} \tag{3.2}$$

$$\mathcal{Q} := \mathcal{L}_2(\Omega) \text{ (pressure space)} \tag{3.3}$$

Multiplying each term of the momentum equation by a function $\boldsymbol{w} \in \mathcal{V}$, and the mass equation by $r \in \mathcal{Q}$, take the integral over Ω.
The next step is integrating by parts the viscosity and pressure terms in the momentum equation: notice that the terms appearing on the boundary vanish due to the definition of $\mathcal{V}$.

The weak formulation of the problem is then: find $\boldsymbol{u} \in \mathcal{S}$ and $p \in \mathcal{Q}$, such that

$$\begin{cases} a(\boldsymbol{u}, \boldsymbol{w}) + c(\boldsymbol{u}; \boldsymbol{w}, \boldsymbol{u}) + b(\boldsymbol{w}, p) = (\boldsymbol{b}, \boldsymbol{w}) & \forall \boldsymbol{w} \in \mathcal{V}, \\ b(\boldsymbol{u}, r) = 0 & \forall r \in \mathcal{Q}, \end{cases} \tag{3.4}$$

where the various terms are:

- The bilinear forms:

$$\begin{aligned} a(\boldsymbol{u}, \boldsymbol{w}) &= \frac{1}{\mathrm{Re}} \int_\Omega \nabla \boldsymbol{w} : \nabla \boldsymbol{u} \quad d\Omega \\ b(\boldsymbol{w}, p) &= -\int_\Omega p \nabla \cdot \boldsymbol{w} \quad d\Omega \\ b(\boldsymbol{u}, r) &= -\int_\Omega r \nabla \cdot \boldsymbol{u} \quad d\Omega \end{aligned}$$

- The linear form:

$$f = (\boldsymbol{b}, \boldsymbol{w})$$

- And the trilinear form, characterizing the Navier-Stokes problem:

$$c(\boldsymbol{a}; \boldsymbol{w}, \boldsymbol{u}) = (\boldsymbol{w}, (\boldsymbol{a} \cdot \nabla)\boldsymbol{u}) = \int_\Omega (\boldsymbol{w} \cdot (\boldsymbol{a} \cdot \nabla)\boldsymbol{u})\, d\Omega,$$

which is associated with the nonlinear convective term in the momentum equation.
Now define the spaces $\mathcal{T} = \{T \in \mathcal{H}^1_{T_D}(\Omega)\}$ and $\mathcal{W} = \{W \in \mathcal{H}^1_0(\Omega)\}$. Following the same reasoning that brought to system (3.4), multiply each term of equation (2.2) by W and take the integral on Ω of both sides. Integrating by parts and applying the boundary conditions, it is possible to obtain the weak form of the problem: find $T \in \mathcal{T}$ s.t.

$$\text{Re Pr} \int_\Omega (\boldsymbol{u} \cdot \nabla) T W d\Omega + \int_\Omega \beta(\phi)(1-T) W d\Omega + \int_\Omega \nabla T \cdot \nabla W d\Omega = 0 \quad \forall W \text{ in } \mathcal{W} \tag{3.5}$$

The Lagrangian of the problem is defined as

$$\mathcal{L} = J + \int_\Omega (\mathbf{R}_{\boldsymbol{u}} \cdot \boldsymbol{w})\, d\Omega + \int_\Omega (\mathbf{R}_p r)\, d\Omega + \int_\Omega (\mathbf{R}_T W)\, d\Omega$$

$\mathbf{R}_{\boldsymbol{u}}, \mathbf{R}_p, \mathbf{R}_T$ are the residuals of the equations of momentum, mass, and heat respectively, and $\boldsymbol{w}, r, W$ are the corresponding test functions, doubling down as adjoint variables. From the point of view of the Lagrangian, they are acting as Lagrange multipliers.
There are $2d + 5$ equations that a point in the space $(\phi, \boldsymbol{u}, p, T, \boldsymbol{w}, r, W)$ must satisfy, to be a critical point of the Lagrangian. Calling $\boldsymbol{v}, q, S$ the test functions the derivatives of the Lagrangian will be tested against, if $d = 2$, this leads to:

$$\begin{aligned}
&\left(\frac{\partial \mathcal{L}}{\partial \boldsymbol{w}}, \boldsymbol{v}\right) = 0, \quad \left(\frac{\partial \mathcal{L}}{\partial r}, q\right) = 0, \quad \left(\frac{\partial \mathcal{L}}{\partial W}, S\right) = 0, \\
&\left(\frac{\partial \mathcal{L}}{\partial \boldsymbol{u}}, \boldsymbol{v}\right) = 0, \quad \left(\frac{\partial \mathcal{L}}{\partial p}, q\right) = 0, \quad \left(\frac{\partial \mathcal{L}}{\partial T}, S\right) = 0, \\
&\left(\frac{\partial \mathcal{L}}{\partial \phi}, \psi\right) = 0,
\end{aligned}$$

3.2 Recover the state equations

In order to check that the Lagrangian is built correctly, the derivative of $\mathcal{L}$ with respect to the adjoint variables are computed, recovering the state equations of the problem.
It is easy to see that

$$\begin{aligned}
\left(\frac{\partial \mathcal{L}}{\partial \boldsymbol{w}}, \boldsymbol{v}\right) &= \int_\Omega (\mathbf{R}_{\boldsymbol{u}} \cdot \boldsymbol{v})\, d\Omega \\
\left(\frac{\partial \mathcal{L}}{\partial r}, q\right) &= \int_\Omega (\mathbf{R}_p q)\, d\Omega \\
\left(\frac{\partial \mathcal{L}}{\partial W}, S\right) &= \int_\Omega (\mathbf{R}_T S)\, d\Omega
\end{aligned}$$

Considering that these hold for any test function and that these terms all equate to 0, that is

$$\begin{aligned}
&\mathbf{R}_{\boldsymbol{u}} = (\boldsymbol{u} \cdot \nabla)\boldsymbol{u} - \frac{1}{\text{Re}} \nabla^2 \boldsymbol{u} + \nabla p + \alpha \boldsymbol{u} = \mathbf{0} && \text{in } \Omega, \\
&\mathbf{R}_p = -\nabla \cdot \boldsymbol{u} = 0 && \text{in } \Omega, \\
&\mathbf{R}_T = \text{Re Pr}\, (\boldsymbol{u} \cdot \nabla) T - \Delta T - \beta(1-T) = 0 && \text{in } \Omega,
\end{aligned} \tag{3.6}$$

And the state equations are recovered.

3.3 Compute the adjoint equations

Now the adjoint problem will be derived, as its solution will be needed for the topology optimization algorithm. Starting from the conditions for criticality, take the derivatives of the Lagrangian w.r.t. the state variables and obtain the weak form of the adjoint problem; then move to the strong form integrating by parts, thus obtaining the adjoint boundary conditions.
The first variable to be tackled is pressure, yielding

$$\left(\frac{\partial \mathcal{L}}{\partial p}, q\right) = \int_\Omega (\boldsymbol{w} \cdot \nabla q)\, d\Omega = 0 \tag{3.7}$$

For the adjoint temperature, it holds

$$\left(\frac{\partial \mathcal{L}}{\partial T}, S\right) = -\int_\Omega \left(W \nabla^2 S\right) d\Omega + \text{Re Pr} \int_\Omega (W \boldsymbol{u} \cdot \nabla S)\, d\Omega + \int_\Omega (\beta(\phi) W S)\, d\Omega + \int_\Omega \frac{\partial J}{\partial T} S d\Omega = 0 \tag{3.8}$$

where the last term is the derivative of the objective functional w.r.t T.
Moving to velocity, and beginning with the non-linear term, Taylor's frozen turbulence approximation [40] is used to simplify computations. This approach yields

$$\left(\frac{\partial \mathcal{L}}{\partial \boldsymbol{u}}, \boldsymbol{v}\right) = \int_\Omega \boldsymbol{w} \cdot \left[(\boldsymbol{v}\cdot\nabla)\boldsymbol{u} + (\boldsymbol{u}\cdot\nabla)\boldsymbol{v} - \frac{1}{\mathrm{Re}}\nabla^2\boldsymbol{v} + \alpha(\phi)\,\boldsymbol{v}\right] d\Omega - \int_\Omega r\nabla\cdot\boldsymbol{v} d\Omega + \mathrm{Re}\ \mathrm{Pr}\int_\Omega W\nabla T\cdot\boldsymbol{v} d\Omega \quad (3.9)$$

Applying integration by parts and divergence theorem repeatedly in order to obtain the strong form of the adjoint problem is an essential step, as it is used to derive the boundary conditions that the adjoint variables need to fulfill. Start with pressure at equation (3.7):

$$\int_\Omega (\boldsymbol{w}\cdot\nabla q)\, d\Omega = \int_{\partial\Omega} q\boldsymbol{w}\cdot\boldsymbol{n} d\partial\Omega - \int_\Omega q\nabla\cdot\boldsymbol{w} d\Omega$$

For equation 3.8, the Laplacian term needs to be integrated twice:

$$-\int_\Omega \left(W\nabla^2 S\right) d\Omega = \int_{\partial\Omega} \left(S(\nabla W\cdot\boldsymbol{n}) - W(\nabla S\cdot\boldsymbol{n})\right) d\partial\Omega - \int_\Omega S\nabla^2 W d\Omega \quad (3.10)$$

The convective term can be recast as:

$$\mathrm{Re}\ \mathrm{Pr}\int_\Omega (W\boldsymbol{u}\cdot\nabla S)\, d\Omega = \mathrm{Re}\ \mathrm{Pr}\left[\int_{\partial\Omega} SW\boldsymbol{u}\cdot\boldsymbol{n} d\partial\Omega - \cancel{\int_\Omega SW(\nabla\cdot\boldsymbol{u})\, d\Omega} - \int_\Omega SW\cdot\nabla\boldsymbol{u} d\Omega\right] \quad (3.11)$$

where the middle term is canceled due to the incompressibility of the fluid.
In the adjoint momentum equation (3.9), integrate twice the viscosity term, and obtain

$$-\int_\Omega \frac{1}{\mathrm{Re}}\nabla^2\boldsymbol{v}\cdot\boldsymbol{w} d\Omega = -\frac{1}{\mathrm{Re}}\left[\int_\Gamma ((\nabla\boldsymbol{v})\,\boldsymbol{w} - (\nabla\boldsymbol{w})\,\boldsymbol{v})\cdot\boldsymbol{n} d\Gamma + \int_\Omega \nabla^2\boldsymbol{w}\cdot\boldsymbol{v} d\Omega\right] \quad (3.12)$$

The pressure coupling term yields

$$\int_\Omega r\nabla\cdot\boldsymbol{v} d\Omega = \int_\Gamma r(\boldsymbol{v}\cdot\boldsymbol{n})\, d\Gamma - \int_\Omega \nabla r\cdot\boldsymbol{v} d\Omega \quad (3.13)$$

The last term that needs to be integrated is the velocity convection arising from the non-linear term in Navier-Stokes:

$$\int_\Gamma [\boldsymbol{n}(\boldsymbol{w}\cdot\boldsymbol{u}) + \boldsymbol{w}(\boldsymbol{u}\cdot\boldsymbol{n})]\cdot\boldsymbol{v} d\Gamma - \int_\Omega \left(\nabla^T\boldsymbol{w}\cdot\boldsymbol{u} + (\boldsymbol{u}\cdot\nabla)\boldsymbol{w}\right)\cdot\boldsymbol{v} d\Omega \quad (3.14)$$

All the computations developed so far amount to the adjoint problem in strong form, with boundary conditions expressed in integral form:

$$-(\boldsymbol{u}\cdot\nabla)\boldsymbol{w} - \nabla^T\boldsymbol{w}\cdot\boldsymbol{u} + \nabla q - \nabla\cdot(\nu\nabla\boldsymbol{w}) + \alpha\boldsymbol{w} + \mathrm{Re}\ \mathrm{Pr}W\nabla T = -\frac{\partial J_\Omega}{\partial \boldsymbol{u}} \text{ on } \Omega \quad (3.15a)$$

$$-\nabla\cdot\boldsymbol{w} = -\frac{\partial J_\Omega}{\partial p} \text{ on } \Omega \quad (3.15b)$$

$$-\nabla^2 W - \mathrm{Re}\ \mathrm{Pr}(\boldsymbol{u}\cdot\nabla)W + \beta(\phi)W = -\frac{\partial J_\Omega}{\partial T} \text{ on } \Omega \quad (3.15c)$$

$$\int_{\partial\Omega} [\boldsymbol{n}(\boldsymbol{w}\cdot\boldsymbol{u}) + \boldsymbol{w}(\boldsymbol{u}\cdot\boldsymbol{n})]\cdot\boldsymbol{v} d\partial\Omega - \int_{\partial\Omega} r(\boldsymbol{v}\cdot\boldsymbol{n})\, d\partial\Omega - \frac{1}{\mathrm{Re}}\int_{\partial\Omega} ((\nabla\boldsymbol{v})\,\boldsymbol{w} - (\nabla\boldsymbol{w})\,\boldsymbol{v})\cdot\boldsymbol{n} d\partial\Omega = -\int_{\partial\Omega} \frac{\partial J_\Gamma}{\partial \boldsymbol{u}}\cdot\boldsymbol{v} d\partial\Omega \quad (3.15d)$$

$$\int_{\partial\Omega} q\boldsymbol{w}\cdot\boldsymbol{n} d\partial\Omega = -\int_{\partial\Omega} \frac{\partial J_\Gamma}{\partial p} q d\partial\Omega \quad (3.15e)$$

$$\int_{\partial\Omega} \left(S(\nabla W\cdot\boldsymbol{n}) - W(\nabla S\cdot\boldsymbol{n})\right) d\partial\Omega + \mathrm{Re}\ \mathrm{Pr}\int_{\partial\Omega} SW\boldsymbol{u}\cdot\boldsymbol{n} d\partial\Omega = -\int_{\partial\Omega} \frac{\partial J_\Gamma}{\partial T} S d\partial\Omega \quad (3.15f)$$

3.3.1 Particularization to ducted flows

All the case studies presented in this work are examples of two-dimensional laminar ducted flows: these are flows with low-to-moderate Reynolds number, in which the boundary can be divided in *inlet(s)* Γ_{in}, *outlet(s)* Γ_{out}, and *walls* Γ_{w}.
This knowledge can be used to particularize the equations defining the boundary conditions for the adjoint problem, (3.15d) to (3.15f). The computations carried out in this section follow [41] and [27]

- **Inlet**:

The conditions for the primal variables are:

$$\begin{cases} \boldsymbol{u} = (u_{\text{int}}, 0) \\ T = 0 \end{cases} \tag{3.16}$$

This implies $\boldsymbol{v} = \boldsymbol{0}$ and $S = 0$ and thus equations (3.15d) to (3.15f) become

$$-\frac{1}{\text{Re}} \int_{\Gamma_{\text{in}}} (\boldsymbol{n} \cdot \nabla \boldsymbol{v})\, \boldsymbol{w} d\Gamma = \boldsymbol{0} \tag{3.17a}$$

$$\int_{\Gamma_{\text{in}}} q\boldsymbol{w} \cdot \boldsymbol{n} d\Gamma = -\int_{\Gamma_{\text{in}}} \frac{\partial J_\Gamma}{\partial p} q d\Gamma \tag{3.17b}$$

$$-\int_{\Gamma_{\text{in}}} (W\, (\nabla S \cdot \boldsymbol{n}))\, d\Gamma = 0 \tag{3.17c}$$

The first equation can be written in its tangential ($\parallel$) and orthogonal ($\perp$) component, using the fact that $0 = \nabla \cdot \boldsymbol{v} = (\boldsymbol{n} \cdot \nabla) v_\perp + \nabla_\parallel \cdot \boldsymbol{v}_\parallel$. This equation leads to $(\boldsymbol{n} \cdot \nabla) v_\perp = 0$ and therefore $(\boldsymbol{n} \cdot \nabla)\boldsymbol{v} = (\boldsymbol{n} \cdot \nabla)\boldsymbol{v}_\parallel$. The momentum equation becomes $-\frac{1}{\text{Re}} \int_{\Gamma_{\text{in}}} \left(\boldsymbol{n} \cdot \nabla \boldsymbol{v}_\parallel\right) \boldsymbol{w}_\parallel d\Gamma = \boldsymbol{0}$ on the inlet. Since the equations found must hold for any $\boldsymbol{v}, q$ and S, what computed so far implies

$$\boldsymbol{w}_\parallel = \boldsymbol{0} \tag{3.18a}$$

$$\boldsymbol{w}_\perp = -\frac{\partial J_\Gamma}{\partial p} \cdot \boldsymbol{n} \tag{3.18b}$$

$$W = 0 \tag{3.18c}$$

- **Walls**:

The conditions for the primal variables are:

$$\begin{cases} \boldsymbol{u} = \boldsymbol{0} \\ \nabla T \cdot \boldsymbol{n} = 0 \end{cases} \tag{3.19}$$

This implies $\boldsymbol{v} = \boldsymbol{0}$ and $\nabla S \cdot \boldsymbol{n} = 0$ and thus equations (3.15d) to (3.15f) become

$$-\frac{1}{\text{Re}} \int_{\Gamma_{\text{w}}} (\boldsymbol{n} \cdot \nabla \boldsymbol{v})\, \boldsymbol{w} d\Gamma = \boldsymbol{0} \tag{3.20a}$$

$$\int_{\Gamma_{\text{w}}} q\boldsymbol{w} \cdot \boldsymbol{n} d\Gamma = -\int_{\Gamma_{\text{w}}} \frac{\partial J_\Gamma}{\partial p} q d\Gamma \tag{3.20b}$$

$$\int_{\Gamma_{\text{w}}} S\, (\nabla W \cdot \boldsymbol{n})\, d\Gamma_{\text{w}} + \text{Re Pr} \int_{\Gamma_{\text{w}}} SW\boldsymbol{u} \cdot \boldsymbol{n} d\Gamma = -\int_{\Gamma_{\text{w}}} \frac{\partial J_\Gamma}{\partial T} S d\Gamma \tag{3.20c}$$

The same reasoning that led to the boundary conditions for adjoint velocity on the inlet leads to:

$$\boldsymbol{w}_\parallel = \boldsymbol{0}, \tag{3.21a}$$

$$\boldsymbol{w}_\perp = -\frac{\partial J_\Gamma}{\partial p}. \tag{3.21b}$$

$$(\nabla W \cdot \boldsymbol{n}) + \text{Re Pr} W\boldsymbol{u} \cdot \boldsymbol{n} = -\frac{\partial J_\Gamma}{\partial T}. \tag{3.21c}$$

- **Outlet**:

The condition

$$\begin{cases} \boldsymbol{n} \left(\frac{1}{\text{Re}} \nabla \boldsymbol{u} - p\text{I}\right) = 0 \\ \nabla T \cdot \boldsymbol{n} = 0 \end{cases} \tag{3.22}$$

implies $(\boldsymbol{n}\cdot\nabla)\boldsymbol{v}=\boldsymbol{0}$ and $\nabla S\cdot\boldsymbol{n}=0$ and thus equations (3.15d) to (3.15f) become

$$\int_{\Gamma_{\text{out}}}[\boldsymbol{n}(\boldsymbol{w}\cdot\boldsymbol{u})+\boldsymbol{w}(\boldsymbol{u}\cdot\boldsymbol{n})]\cdot\boldsymbol{v}d\Gamma-\int_{\Gamma_{\text{out}}}r\,(\boldsymbol{v}\cdot\boldsymbol{n})\,d\Gamma+\frac{1}{\text{Re}}\int_{\Gamma_{\text{out}}}(\nabla\boldsymbol{w})\,\boldsymbol{v}\cdot\boldsymbol{n}d\Gamma=-\int_{\Gamma_{\text{out}}}\frac{\partial J_\Gamma}{\partial\boldsymbol{u}}\cdot\boldsymbol{v}d\Gamma, \tag{3.23a}$$

$$\int_{\Gamma_{\text{out}}}q\boldsymbol{w}\cdot\boldsymbol{n}d\Gamma=-\int_{\Gamma_{\text{out}}}\frac{\partial J_\Gamma}{\partial p}qd\Gamma, \tag{3.23b}$$

$$\int_{\Gamma_{\text{out}}}S\,(\nabla W\cdot\boldsymbol{n})\,d\Gamma+\text{Re Pr}\int_{\Gamma_{\text{out}}}SW\boldsymbol{u}\cdot\boldsymbol{n}d\Gamma=-\int_{\Gamma_{\text{out}}}\frac{\partial J_\Gamma}{\partial T}Sd\Gamma. \tag{3.23c}$$

These integral conditions translate to the following Neumann condition:

$$[\boldsymbol{n}(\boldsymbol{w}\cdot\boldsymbol{u})+\boldsymbol{w}(\boldsymbol{u}\cdot\boldsymbol{n})]-r\boldsymbol{n}+\frac{1}{\text{Re}}(\nabla\boldsymbol{w})\,\boldsymbol{n}=-\frac{\partial J_\Gamma}{\partial\boldsymbol{u}} \tag{3.24a}$$

$$(\nabla W\cdot\boldsymbol{n})+\text{Re PrW}\boldsymbol{u}\cdot\boldsymbol{n}=-\frac{\partial J_\Gamma}{\partial T} \tag{3.24b}$$

The boundary conditions for any objective functional have therefore been determined. Notice that if $J_\Omega=0$, as it is often the case in topology optimization, then the adjoint problem only depends on the objective functional through the boundary conditions and therefore changes in the cost J don't imply the computation of a costly matrix.

3.3.2 Pressure drop and heat dissipation objective functionals

The heat flux at the solid-fluid interface is notoriously difficult to compute in such problems and therefore methods using the temperature field to estimate the heat exchange are common in the literature [42], [12]. This work adopts one such method, proposed by [30], that consists in defining

$$J_T=-\int_\Omega\beta(1-T)d\Omega$$

Another relevant quantity in the industrial design of fluid-cooled heat exchangers is the total pressure drop between inlet and outlet, expressed by the functional

$$J_{\boldsymbol{u}}=-\int_{\Gamma_{\text{in}}\cup\Gamma_{\text{out}}}\left(p+\frac{1}{2}|u|^2\right)(u\cdot n)d\Gamma$$

In Appendix A, it is proved that this is equivalent to defining

$$J_{\boldsymbol{u}}=\int_\Omega\left(\frac{1}{\text{Re}}\nabla\boldsymbol{u}:\nabla\boldsymbol{u}+\alpha\boldsymbol{u}\cdot\boldsymbol{u}\right)d\Omega$$

Despite the advantages mentioned in the previous subsection, in this case it is useful to formulate the problem in terms of functionals defined on the domain. As a consequence this work will hereafter consider the latter definition of $J_{\boldsymbol{u}}$.

A possible approach to the concurrent optimization of both objectives is the *weighted sum* method.
Define the objective functional

$$J=\nu J_T+(1-\nu)J_{\boldsymbol{u}} \tag{3.25}$$

where $\nu\in\mathbb{R}:0<\nu<1$ is a scalar acting as a weight that regulates the relative importance of the two concurring objectives.
With these definitions, it becomes possible to evaluate some quantities exactly, namely

$$\begin{aligned}
&\left(\frac{\partial J_\Gamma}{\partial\boldsymbol{u}},\boldsymbol{v}\right)=0,\\
&\left(\frac{\partial J_\Gamma}{\partial p},q\right)=\boldsymbol{0},\\
&\left(\frac{\partial J_\Gamma}{\partial T},S\right)=\boldsymbol{0},\\
&\left(\frac{\partial J_\Omega}{\partial\boldsymbol{u}},\boldsymbol{v}\right)=\int_\Omega 2(1-\nu)\left(\frac{1}{\text{Re}}\nabla\boldsymbol{u}:\nabla\boldsymbol{v}+\alpha\boldsymbol{u}\cdot\boldsymbol{v}\right)d\Omega,\\
&\left(\frac{\partial J_\Omega}{\partial p},q\right)=\boldsymbol{0},\\
&\left(\frac{\partial J_\Omega}{\partial T},S\right)=\int_\Omega\nu\beta Sd\Omega.
\end{aligned} \tag{3.26}$$

Hence, the adjoint problem becomes

$$-(\boldsymbol{u}\cdot\nabla)\boldsymbol{w}-\nabla^T\boldsymbol{w}\cdot\boldsymbol{u}+\nabla q-\nabla\cdot(\nu\nabla\boldsymbol{w})+\alpha\boldsymbol{w}=-\text{Re Pr}W\nabla T+2(1-\nu)\left(\frac{1}{\text{Re}}\nabla^2\boldsymbol{u}-\alpha\boldsymbol{u}\right) \quad \text{on } \Omega, \tag{3.27a}$$

$$-\nabla\cdot\boldsymbol{w}=0 \text{ on } \Omega, \tag{3.27b}$$

$$-\nabla^2 W-\text{Re Pr}\,(\boldsymbol{u}\cdot\nabla)W+\beta W=-\nu\beta \quad \text{on } \Omega, \tag{3.27c}$$

$$\boldsymbol{w}=\boldsymbol{0} \text{ in } \Gamma_{\text{in}}\cup\Gamma_{\text{w}}, \tag{3.27d}$$

$$[\boldsymbol{n}(\boldsymbol{w}\cdot\boldsymbol{u})+\boldsymbol{w}(\boldsymbol{u}\cdot\boldsymbol{n})]-r\boldsymbol{n}+\frac{1}{\text{Re}}(\nabla\boldsymbol{w})\,\boldsymbol{n}=\boldsymbol{0} \quad \text{in } \Gamma_{\text{out}}, \tag{3.27e}$$

$$W=0 \quad \text{in } \Gamma_{\text{in}}, \tag{3.27f}$$

$$(\nabla W\cdot\boldsymbol{n})+\text{Re Pr}W\boldsymbol{u}\cdot\boldsymbol{n}=0 \quad \text{in } \Gamma_{\text{w}}, \tag{3.27g}$$

$$(\nabla W\cdot\boldsymbol{n})+\text{Re Pr}W\boldsymbol{u}\cdot\boldsymbol{n}=0 \quad \text{in } \Gamma_{\text{out}}. \tag{3.27h}$$

3.4 Sensitivities

In order to obtain the sensitivities, consider that $\alpha'(\phi)=(\zeta-1)(\alpha_{\max}-\alpha_{\min})\phi^{\zeta-1}$ and $\beta'(\phi)=(\zeta-1)(\beta_{\max}-\beta_{\min})\phi^{\zeta-1}$. Then the sensitivity of the objective functional with respect to the design variable is given by

$$\begin{aligned}\langle J'(\phi,\boldsymbol{u},p,T),\psi\rangle=&\left\langle\frac{\partial\mathcal{L}}{\partial\phi}(\phi,\boldsymbol{u},\boldsymbol{w},p,r,T,W),\psi\right\rangle+\left\langle\frac{\partial\mathcal{L}}{\partial\boldsymbol{u}}(\phi,\boldsymbol{u},\boldsymbol{w},p,r,T,W),\langle\boldsymbol{u}'(\phi),\psi\rangle\right\rangle+\\&\left\langle\frac{\partial\mathcal{L}}{\partial\boldsymbol{w}}(\phi,\boldsymbol{u},\boldsymbol{w},p,r,T,W),\langle\boldsymbol{w}'(\phi),\psi\rangle\right\rangle+\left\langle\frac{\partial\mathcal{L}}{\partial p}(\phi,\boldsymbol{u},\boldsymbol{w},p,r,T,W),\langle p'(\phi),\psi\rangle\right\rangle+\\&\left\langle\frac{\partial\mathcal{L}}{\partial r}(\phi,\boldsymbol{u},\boldsymbol{w},p,r,T,W),\langle r'(\phi),\psi\rangle\right\rangle+\left\langle\frac{\partial\mathcal{L}}{\partial T}(\phi,\boldsymbol{u},\boldsymbol{w},p,r,T,W),\langle T'(\phi),\psi\rangle\right\rangle+\\&\left\langle\frac{\partial\mathcal{L}}{\partial U}(\phi,\boldsymbol{u},\boldsymbol{w},p,r,T,W),\langle W'(\phi),\psi\rangle\right\rangle\end{aligned} \tag{3.28}$$

It is possible to identify the right term of each braket with a test function as $\boldsymbol{v}=\langle\boldsymbol{u}'(\phi),\psi\rangle$ and similarly for the other variables. This way, every term but the very first one corresponds either to the state or adjoint constraints and it is thus identically 0.

Therefore, equation 3.28 becomes

$$J'=\alpha'\boldsymbol{u}\cdot\boldsymbol{w}+(1-\nu)\alpha'\boldsymbol{u}\cdot\boldsymbol{u}-\beta'(1-T)(\nu+W) \tag{3.29}$$

Chapter 4

RDE-based topology optimization of a coupled thermal-fluid problem

4.1 Discrete form of the state equations

Introduce the finite dimensional subspaces $\mathcal{S}^h, \mathcal{V}^h$ and $\mathcal{Q}^h$, discretization of (3.1), (3.2) and (3.3), respectively. The interpolation spaces for velocity and pressure are chosen as the Taylor-Hood couple P2/P1. This couple is notoriously LBB compliant [38] and no stabilization scheme will therefore be needed. Substituting the continuous functions with their discrete counterparts in (3.4) and (3.5), it is possible to obtain the Galerkin formulation of the Navier-Stokes and the coupled heat transfer problem. Define $\boldsymbol{v}_D^h \in \mathcal{S}^h$ such that $\boldsymbol{v}^h = \boldsymbol{u}^h + \boldsymbol{v}_D^h$, then find the auxiliary velocity field $\boldsymbol{u}^h \in \mathcal{V}^h$ and the pressure $p^h \in \mathcal{Q}^h$, such that, for all $\left(\boldsymbol{v}^h, q^h\right) \in \mathcal{V}^h \times \mathcal{Q}^h$,

$$\begin{cases} a\left(\boldsymbol{u}^h, \boldsymbol{v}^h\right) + c\left(\boldsymbol{u}^h; \boldsymbol{v}^h, \boldsymbol{u}^h\right) + b\left(\boldsymbol{v}^h, p^h\right) = \left(\boldsymbol{b}^h, \boldsymbol{v}^h\right) - a\left(\boldsymbol{u}_D^h, \boldsymbol{v}^h\right) - c\left(\boldsymbol{u}^h; \boldsymbol{v}^h, \boldsymbol{u}_D^h\right) \\ b\left(\boldsymbol{u}^h, q^h\right) = -b\left(\boldsymbol{u}_D^h, q^h\right) \end{cases}$$

with the bilinear forms defined in (3.1).
Note that now, the r.h.s. term depends on the unknown because $\boldsymbol{v}^h = \boldsymbol{u}^h + \boldsymbol{v}_D^h$. These terms combine into the nonlinear system

$$\begin{pmatrix} \mathbf{K} + \mathbf{C}(\boldsymbol{u}) & \mathbf{G} \\ \mathbf{G}^T & \mathbf{0} \end{pmatrix} \begin{pmatrix} \boldsymbol{u} \\ \mathbf{p} \end{pmatrix} = \begin{pmatrix} \mathbf{f}(\boldsymbol{u}) \\ \mathbf{h} \end{pmatrix}$$

which can be solved with a nonlinear iterative method, like Newton-Raphson. The details of its design and implementation are discussed in Appendix B.

In order to obtain the discrete form of the energy equation it is possible to consider $\boldsymbol{u}^h$ as a given field, having already obtained the solution of the previous problem. Following the same approach, define T^h, S^h, and T_D^h in the appropriate spaces, and write the problem as

$$\text{Re Pr} \int_\Omega \left(\boldsymbol{u}^h \cdot \nabla\right) T^h s^h d\Omega - \int_\Omega \beta(\phi)(1-T^h)s^h d\Omega + \int_\Omega \nabla T^h \cdot \nabla s^h d\Omega = -\text{Re Pr} \int_\Omega \left(\boldsymbol{u}^h \cdot \nabla\right) T_D^h s^h d\Omega - \int_\Omega \beta(\phi) T_D^h s^h d\Omega - \int_\Omega \nabla T_D^h \tag{4.1}$$

The chosen interpolation space is P1 and this problem is thus equivalent to the solution of a linear system.

4.2 Treatment of the volume constraint

It is necessary in structural topology optimization ([11], [43]) to introduce a constraint on the maximum fraction of the domain that is allowed to be occupied by the solid. In fluid problems, this constraint is often on the fluid part of the domain instead. Dealing with the problem at hand, convergence to a non-zero, non-unitary fraction of volume is observed naturally due to the form of the objective functional and thus the volume constraint is better seen as acting to aid the convergence [27].

The technique employed is called Augmented Lagrangian [44]. Recalling the definition of $G = \frac{V}{V_0} - V_{req} < 0$, and introducing λ Lagrange multiplier and z parameter, define the augmented Lagrangian

$$\tilde{\mathcal{L}}(\phi, \lambda, z) = J(\phi, \boldsymbol{u}) + \begin{cases} \lambda G(\phi) + \frac{1}{2} z G^2(\phi) & \text{if } G(\phi) \geq -\lambda/z \\ -\frac{\lambda^2}{2z} & \text{if } G(\phi) < -\lambda/z \end{cases} \tag{4.2}$$

The optimal solution is found using an iterative scheme of the kind

$$\phi_{k+1} = \arg\min_{\phi} \tilde{\mathcal{L}}\left(\phi, q_k, z_k\right) \qquad \text{such that } \phi \in [0,1],$$

whereas parameters λ and z are updated at every iteration following [44]

$$\begin{aligned} \lambda_{k+1} &= \lambda_k + z_k \max\left(G(\phi), -\lambda_k/z_k\right), \\ r_{k+1} &= \gamma z_k, \quad \gamma > 1 \end{aligned}$$

With the definition of the augmented Lagrangian the only equation changing in the adjoint formulation is eq. (3.29), where an additional term appears

$$\begin{aligned} &\langle J'(\phi, \boldsymbol{u}, p, T), \psi\rangle = \left\langle \frac{\partial \tilde{\mathcal{L}}}{\partial \phi}(\phi, \boldsymbol{u}, \boldsymbol{w}, p, r, T, W), \psi \right\rangle = \\ &= \alpha' \boldsymbol{u}\cdot\boldsymbol{w} - \beta'(1-T)(\nu+W) + \begin{cases} G'(\phi)(\lambda + zG(\phi)) & \text{if } G(\phi) \geq -\lambda/z \\ 0 & \text{if } G(\phi) < -\lambda/z \end{cases} \end{aligned} \tag{4.3}$$

Since the phase field method incorporates intermediate densities during the iterations, the augmented Lagrangian method is especially suitable as it allows for a sufficiently weak enforcement of the constraint. It is well capable of handling non linear constraints and speed up convergence for ill-conditioned problems, without the need to increase z to infinity.
Since, in principle, the sensitivity can assume very high values due to the factor $\alpha_{\max}$, in order to aid convergence the part of the sensitivity relative to the physics is rescaled to the volume using a factor $\eta = \frac{|\Omega|}{||\omega J'_T + (1-\omega) J'_\omega||_{\mathrm{L}^2(\Omega)}}$.
The sensitivity is therefore redefined as:

$$\begin{aligned} &\langle J'(\phi, \boldsymbol{u}, p, T), \psi\rangle = \left\langle \frac{\partial \tilde{\mathcal{L}}}{\partial \phi}(\phi, \boldsymbol{u}, \boldsymbol{w}, p, r, T, W), \psi \right\rangle = \\ &= \eta\left(\alpha' \boldsymbol{u}\cdot\boldsymbol{w} - \beta'(1-T)(\nu+W)\right) + \begin{cases} G'(\phi)(\lambda + zG(\phi)) & \text{if } G(\phi) \geq -\lambda/z \\ 0 & \text{if } G(\phi) < -\lambda/z \end{cases} \end{aligned} \tag{4.4}$$

4.3 Design variable update scheme

In order to update the variable between iterations, a scheme based on an unsteady reaction-diffusion equation (RDE) proposed by [36] is employed. This approach allows to incorporate a diffusive term, that helps convexifying the optimization problem and is responsible for the smoothing of the borders. Introducing a fictitious time t and the function $\phi \in \Phi$, with $\Phi = \{\phi \in \mathcal{H}^1(\Omega)\}$, the equation in strong form is:

$$\begin{cases} \dfrac{\partial \phi}{\partial t} = \kappa \Delta \phi - J' & \text{in } \Omega \\ \dfrac{\partial \phi}{\partial \boldsymbol{n}} = 0 & \text{on } \Gamma \end{cases} \tag{4.5}$$

This is multiplied by an appropriate test function $\psi \in \Phi$, integrated by parts using the boundary conditions. The problem is discretized in time using an implicit Euler scheme, and in space using a continuous Galerkin scheme, yielding

$$\int_\Omega (\phi_{k+1}\psi) d\Omega - \int_\Omega (\Delta t \kappa \nabla \phi_{k+1} \cdot \nabla \psi) d\Omega = \int_\Omega (\phi_k \psi) d\Omega + \int_\Omega (\Delta t J' \psi) d\Omega \tag{4.6}$$

corresponding to the linear system

$$(\mathrm{M} + \Delta t \mathrm{K})\phi^h_{k+1} = \phi^h_k + \Delta t \mathbf{g} \tag{4.7}$$

with $\mathbf{g}$ representing the right-hand side of equation (4.6)).

4.4 Post-process

4.4.1 Double Well Potential

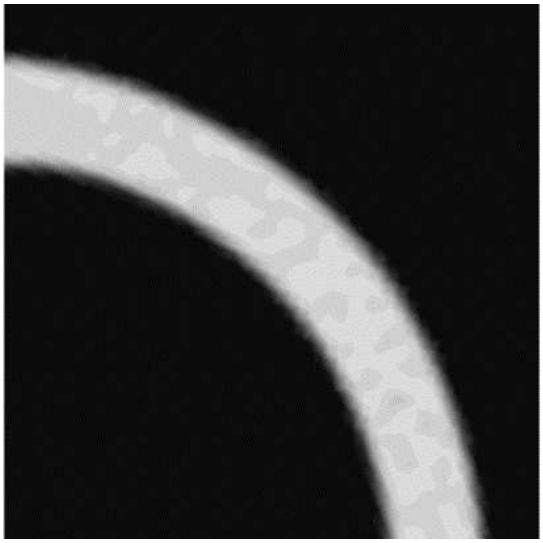

Figure 4.1: Example of solver output: there are visible gray zones in the middle of the duct that make this structure not manifacturable as it currently is.

In figure 4.1 an example of the output of the solver is presented. Some problems plague this result: firstly, the "gray zone" where $0 < \phi < 1$ is too big, extending into the fluid domain. This is caused by the volume constraint. As seen in eq. (4.3), this constraint acts as an additional constant on the sensitivity, assuming the same value on the whole domain. The sensitivity is, however, proportional to the design variable ϕ through α and β. This means that if on iteration i the algorithm empties a patch of solid ($\phi = 0$), at iteration $i + 1$ the part of the sensitivity deriving from the physics is null on the same patch and thus solid is added. The result of this process is that the design variable oscillates on the parts of the domain empty of solid when far from the required fraction of volume.

This undesired behavior can be mitigated slightly setting appropriately the parameters of the Augmented Lagrangian constraint, but most importantly it can be solved through an appropriate post-process procedure. The approach considered in this work is the Double Well Potential (DWP) algorithm, from reference [18]. Define the functions

$$w(\phi) = \phi^2(1-\phi)^2,$$
$$g(\phi) = \phi^3\left(6\phi^2 - 15\phi + 10\right),$$

and

$$J_{\mathrm{DWP}}(\phi) = aw(\phi) + g(\phi)\frac{\partial\tilde{\mathcal{L}}}{\partial\phi}\bigg|_{t=t_1},$$

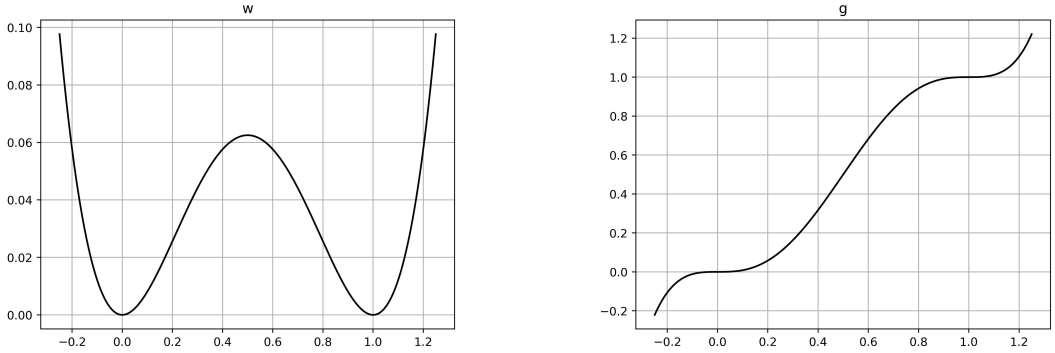

Figure 4.2: Plot of functions $w(\phi)$ and $g(\phi)$, from left to right. $w(\phi)$ has its absolute minima at $\phi = 0$ and $\phi = 1$, and the derivative of $g(\phi)$ is a scaling of w.

The shape of functions w and g is depicted in figure 4.2. Also notice that $g'(\phi) = 30w(\phi)$. Intuitively, the action of $w(\phi)$ encourages the evolution of the design variable towards the values 0 and 1, while penalizing intermediate, "gray" configurations.
This formulation is easily incorporated in the algorithm as it only impacts the sensitivity, and the new derivative is then computed as

$$J'_{\mathrm{DWP}}(\phi) = aw'(\phi) + 30w(\phi)\frac{\partial\tilde{\mathcal{L}}}{\partial\phi}\bigg|_{t=t_1}. \tag{4.8}$$

The equation in strong form thus becomes

$$\begin{cases} \dfrac{\partial\phi}{\partial t} = \kappa\Delta\phi - J'_{\mathrm{DWP}} & \text{in } \Omega \\ \dfrac{\partial\phi}{\partial \boldsymbol{n}} = 0 & \text{on } \Gamma \end{cases} \tag{4.9}$$

Implicit Euler in time and continuous Galerkin in space are used to discretize the problem, yielding

$$\int_\Omega (\phi_{k+1}\psi)d\Omega - \int_\Omega (\Delta t\kappa\nabla\phi_{k+1}\cdot\nabla\psi)d\Omega = \int_\Omega (\phi_k\psi)d\Omega + \int_\Omega (\Delta t J'(\phi_k)\psi)d\Omega \tag{4.10}$$

and the spacial discretization is thus analogous to the previous subsection. The strategy is therefore to run the optimizer to convergence, and then subject the result to a few iterations where the evolution is governed by the DWP-modified equation (4.9).
The result is a figure with an arbitrarily small gray region, limited only by the size of the elements (see figure 4.3).

Figure 4.3: Example of the checkerboard pattern caused by the size of the mesh elements. Manifacture however is not constrained by the size of a mesh, and therefore a result with borders as smooth as possible is to be preferred.

4.4.2 Mesh adaptation

A well-known issue of mesh-based optimization methods is that the accuracy of the optimized geometry is limited by the size of the mesh elements h. This results in jagged borders of the solid domain, entirely due to the inability of the mesh to capture variations at smaller scales. Many solutions have been proposed in the literature such as filtering methods ([14]) but the one adopted by this work is adaptive mesh refinement.

The basic idea is to refine the mesh where the gradient of the solution $\nabla\phi$ is high, leading to very accurate solutions while retaining computability in terms of time and resources. This is even more true for anisotropic mesh adaptation, stretching the elements by different amounts in different directions.
Following [14] the gray zone is measured using the estimator

$$M_{nd} = \frac{\int_{\mathcal{D}} 4\phi(1-\phi)}{|\mathcal{D}|} \times 100$$

The integrand is locally 0 where $\phi = 0$ or $\phi = 1$, and positive where $0 < \phi < 1$. If the domain is filled with gray area ($\phi = 0.5 \ \forall \ (x, y)$), then $M_{nd} = 100\%$.

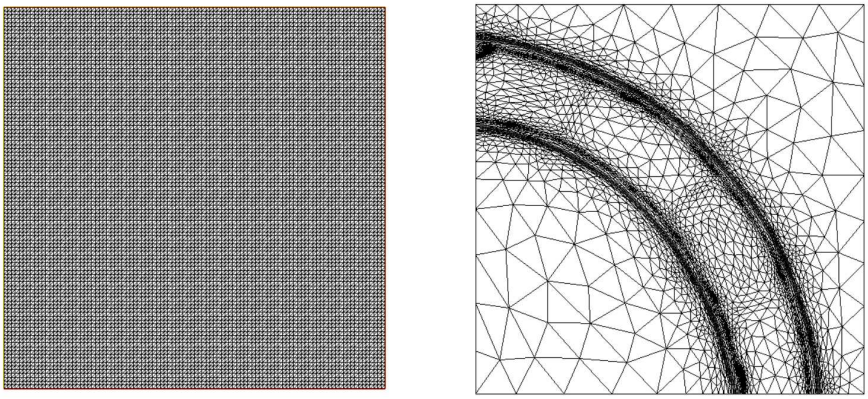

Figure 4.4: Structured vs adapted mesh: notice how approaching the borders of the fluid domain the elements get anisotropically more stretched parallel to the interface, while the mesh gets coarser where ϕ is nearly constant.

The details of the algorithm are explained in Appendix C and the implementation used is taken from [45].

Figure 4.5: Result of the same problem shown in figures 4.1 and 4.3 after the mesh adaptation and the action of the DWP. Further adaptation is possible depending on the precision required by the designer.

As shown in figure 4.5 all the post-process discussed so far amounts to a solution with much better definition and arbitrarily small gray zones, that still takes reasonable times to compute.

Summing everything up, the full algorithm is presented in figure 4.6. The primal and adjoint variables are computed solving the respective problem and the sensitivity is computed. If the volume constraint is not satisfied the algorithm adds the respective term to the sensitivity following the augmented Lagrangian approach and after solving the RDE checks for convergence.

Once the main optimization loop has reached convergence, given by the condition $\frac{||\phi_k^h - \phi_{k-1}^h||_{\mathcal{L}^2(\Omega)}}{||\phi_{k-1}^h||_{\mathcal{L}^2(\Omega)}} < \varepsilon$, a boolean variable is switched and the sensitivity is modified to (4.8), adding the DWP. This second loop is run until the gray zone is under a given threshold. For this work, the thresholds for convergence are set to $\varepsilon = 0.01$ and $M_{nd} < 3\%$.

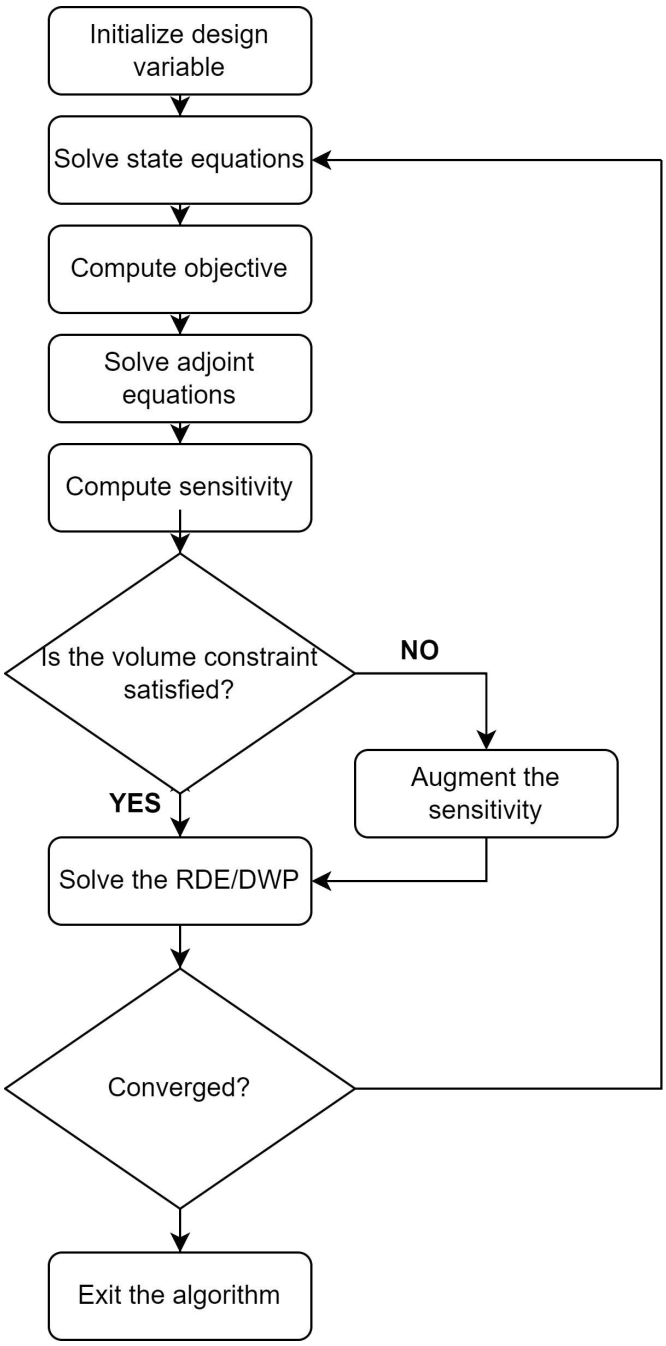

Figure 4.6: Flowchart of the full optimization algorithm

Chapter 5

Numerical results

Since all the code was written in-house it is important to validate the solvers for the state equations, and then the full topology optimization algorithm for the less complex, better known case of minimization of pressure drop. In the rest of this work the following choices for the interpolation spaces are adopted: the Taylor-Hood couple P2/P1 is chosen for the interpolation of velocity and pressure, respectively. This way, the inf-sup condition is satisfied [38], and no spurious oscillations in the pressure field are expected to appear. Temperature T and design variable ϕ are interpolated with P1 basis functions. The adjoint variables are interpolated using the same space of the related primal variable.
All the linear problems appearing in the formulation are solved using a multifrontal method.

5.1 Validation of the solver for the state equations

In this subsection the numerical simulations of known benchmark cases are presented: first, the lid-driven cavity is simulated to validate the Newton-Raphson solver of the Navier-Stokes equation, then the numerical simulation of a flow past a heated cylinder is presented as proof of the correct functioning of the coupled nonlinear solver.

5.1.1 Lid-driven cavity

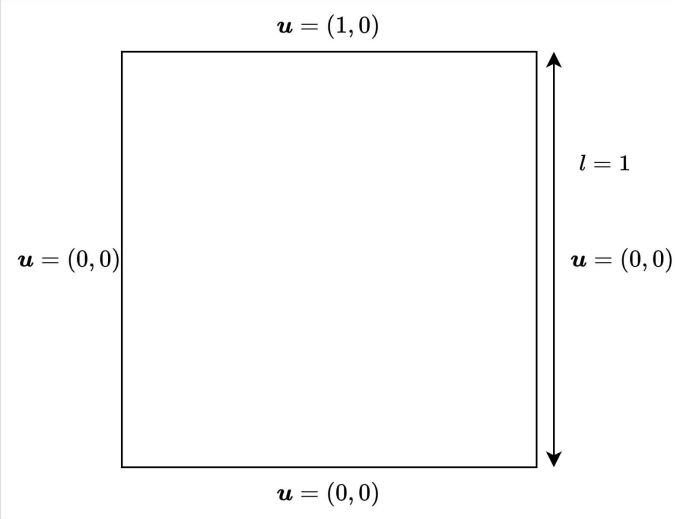

Figure 5.1: Schematics of the test case and the assigned boundary conditions.

With reference to figure 5.1, consider a 2D square domain of unitary side. No slip boundary conditions ($\boldsymbol{u} = \boldsymbol{0}$) are enforced on all sides but the top one $(t, 1) \in \mathbb{R}^2$ s.t. $0 < t < 1$, where the condition $\boldsymbol{u} = (1, 0)$ holds. Under this choice of boundary conditions, pressure is defined up to a constant, and thus the additional condition $\int_\Omega p d\Omega = 0$ is enforced through a Lagrange multiplier to restore uniqueness. Reynolds number is varied between 100 and 1000, and for each case the velocity streamlines are presented. The results are compared to reference [46] in figures 5.2, 5.3 and 5.4. The solutions from the in-house solver are obtained starting from an 80x80 structured mesh of triangular elements.

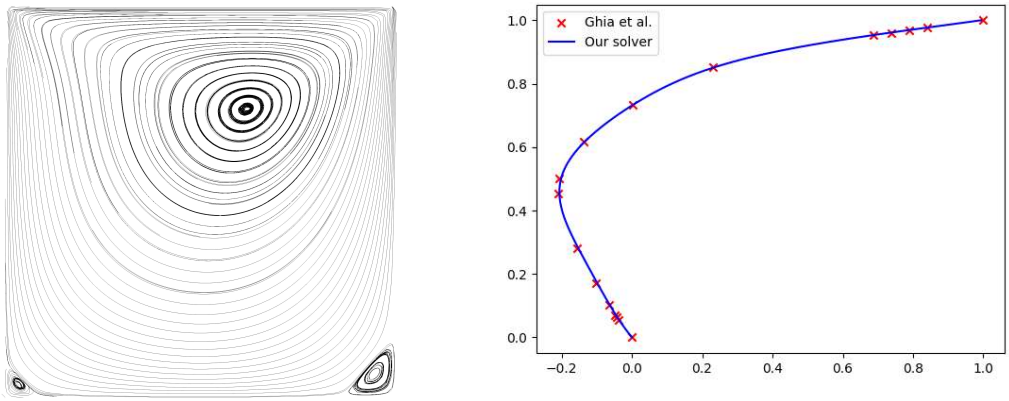

Figure 5.2: Streamlines and pressure for Re = 100

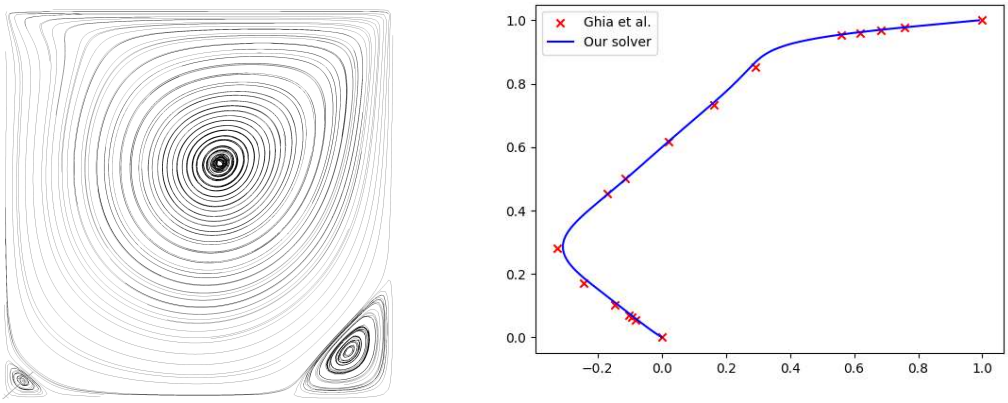

Figure 5.3: Streamlines and pressure for Re = 400

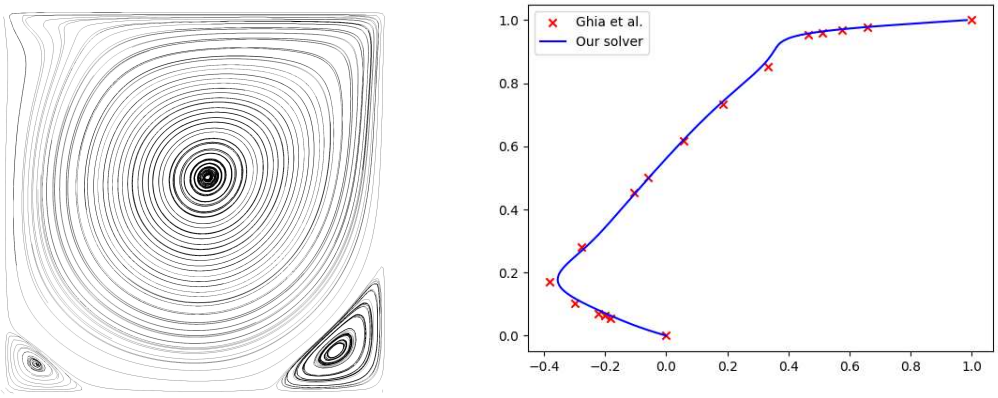

Figure 5.4: Streamlines and pressure for Re = 1000

The plots presented provide numerical proof of the quality of the solver, and it is therefore possible to proceed with the validation of the coupled solver.

5.1.2 Flow past a heated cylinder

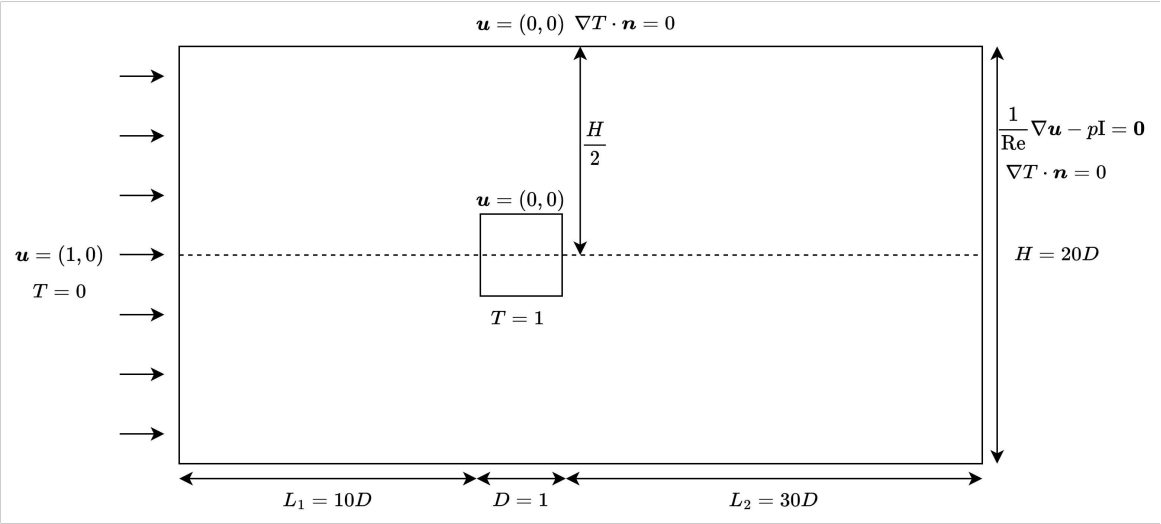

Figure 5.5: Schematics of the test case for the CHT solver

A benchmark for the coupled CHT solver is presented in this subsection, the reference is given by [47]. The problem at hand is the laminar steady flow of a fluid past a heated square cylinder in a rectangular chamber, schematically represented in figure 5.5. The characteristic length is given by the size of the cylinder, set to $D = 1$. The other parameters of the chamber, with reference to the figure, are $H = 20D, L_1 = 10D, L_2 = 30D$. As for the boundary conditions, these are prescribed as: horizontal unitary velocity and null temperature on the inlet, no slip boundary conditions for velocity and homogeneous Neumann for temperature on the walls, and homogeneous Neumann for both velocity and pressure on the outlet. Reynolds number is set to 10 and 40, and Prandtl is set to 0.7 to represent air.
The results presented are computed on an unstructured mesh counting 97126 triangles.

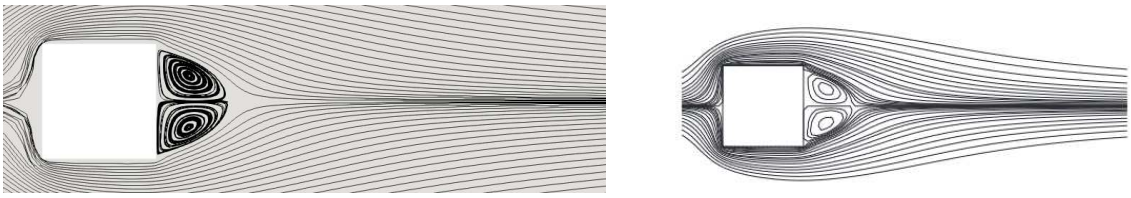

Figure 5.6: Streamlines for Re = 10: results from this work on the left, results from the literature on the right

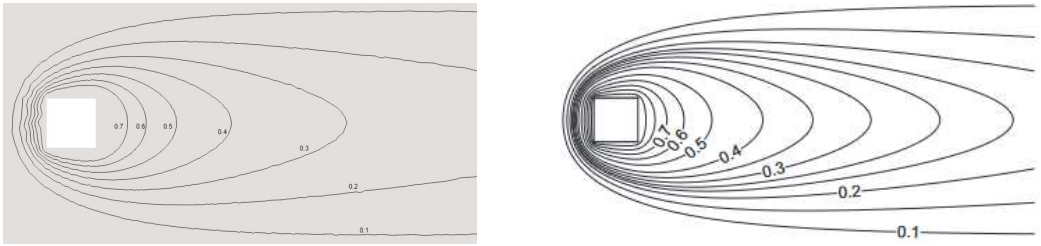

Figure 5.7: Isothermal lines for Re = 10: results from this work on the left, results from the literature on the right

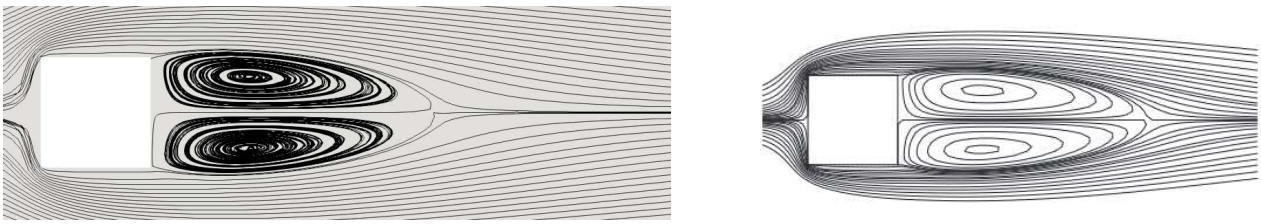

Figure 5.8: Streamlines for Re = 40: results from this work on the left, results from the literature on the right

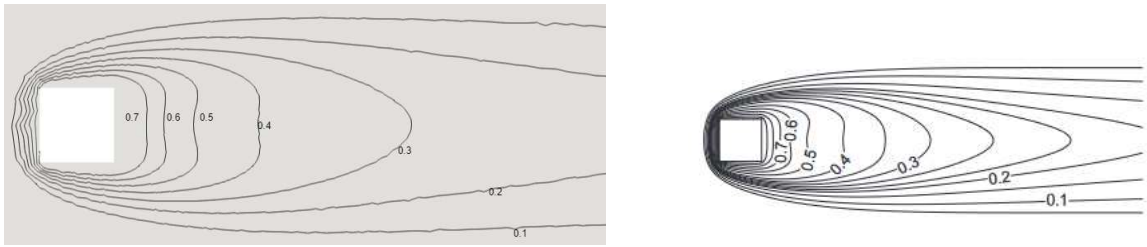

Figure 5.9: Isothermal lines for Re = 40: results from this work on the left, results from the literature on the right

In figures 5.6 to 5.9 streamlines and isothermal lines are compared with the reference.
Notice that the isolines of temperature seem jagged, especially in some parts of the domain. This is not due to numerical oscillations, but the different sizes of the elements before and after the cylinder. In figure 5.10 a zoomed plot of the isothermal lines for Re = 10 is presented, superimposed to the mesh. Comparing the position of the nodes with the jagged lines, it is clear that the slight unevenness of the lines is due to the interpolation error.

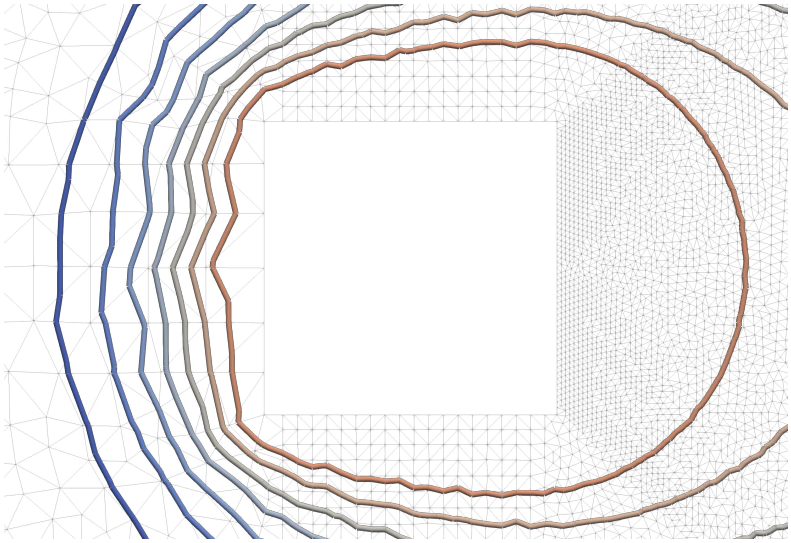

Figure 5.10: Zoomed down plot of isothermal lines for Re = 10. Notice how the size of the elements explains the jaggedness in the lines.

No significant discrepancies have been found between the results presented and the published benchmark, and this proof is thus deemed sufficient to assess the correct functioning of the coupled solver.

5.2 Topology optimization of the pressure drop

The purpose of this section is validating the topology optimizer with a less complex problem, that does not involve temperature. This is the optimization with respect to the objective functional

$$J_{\boldsymbol{u}} = \int_{\Omega} \left(\frac{1}{\mathrm{Re}} \nabla \boldsymbol{u} : \nabla \boldsymbol{u} + \alpha \boldsymbol{u} \cdot \boldsymbol{u} \right) d\Omega$$

In order to achieve this it is possible to set $\nu = 0$ in equation (3.25) and discard the energy equation. The derivation is analogous to the one presented for the coupled problem, except for one term on the right-hand side of the adjoint momentum equation, and one term in the sensitivity.
More precisely, the resulting adjoint equations are:

$$-(\boldsymbol{u}\cdot\nabla)\boldsymbol{w} - \nabla^T\boldsymbol{w}\cdot\boldsymbol{u} + \nabla q - \nabla\cdot(\nu\nabla\boldsymbol{w}) + \alpha\boldsymbol{w} = 2\left(\frac{1}{\mathrm{Re}}\nabla^2\boldsymbol{u} - \alpha\boldsymbol{u}\right) \text{ on } \Omega \tag{5.1a}$$

$$-\nabla\cdot\boldsymbol{w} = 0 \text{ on } \Omega \tag{5.1b}$$

$$\boldsymbol{w} = \boldsymbol{0} \text{ in } \Gamma_{\mathrm{in}}\cup\Gamma_{\mathrm{w}} \tag{5.1c}$$

$$[\boldsymbol{n}(\boldsymbol{w}\cdot\boldsymbol{u}) + \boldsymbol{w}(\boldsymbol{u}\cdot\boldsymbol{n})] - r\boldsymbol{n} + \frac{1}{\mathrm{Re}}(\nabla\boldsymbol{w})\,\boldsymbol{n} = \boldsymbol{0} \text{ in } \Gamma_{\mathrm{out}} \tag{5.1d}$$

and the sensitivity becomes

$$J' = \alpha'\boldsymbol{u}\cdot(\boldsymbol{w}+\boldsymbol{u}) + \begin{cases} G'(\phi)(\lambda + rG(\phi)) & \text{if } G(\phi) \geq -\lambda/r \\ 0 & \text{if } G(\phi) < -\lambda/r \end{cases} \tag{5.2}$$

This obviously implies an analogous redefinition of J_{DWP} and J'_{DWP}.
For this section the optimization parameters are set to $\alpha_{\max} = 2.5\cdot 10^4$, $\alpha_{\min} = 2.5\cdot 10^{-4}$, $\kappa = 10^{-4}$. The augmented Lagrangian parameters are set to $\lambda_0 = 0, z_0 = 0.2, \gamma = 1.025$ Two test cases will be considered for the validation step, the first one being the simple duct case, compared to the results in reference [48].

5.2.1 Simple duct

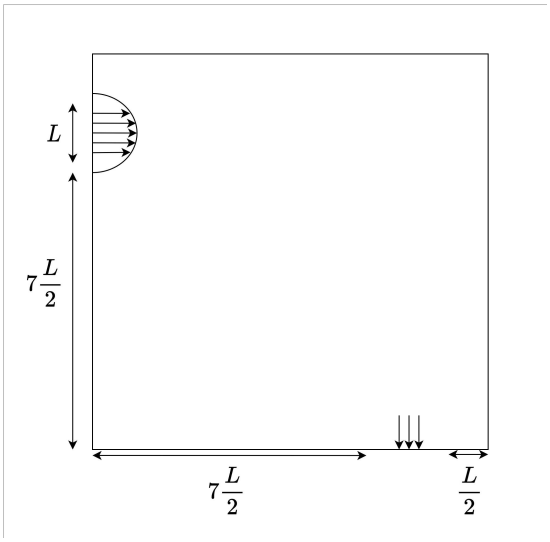

Figure 5.11: Schematics of the test case

In figure 5.11 a schematic representation of the domain and boundary conditions is presented. A sinusoidal velocity profile is enforced on the inlet, with $\boldsymbol{u}_{max} = 1$, in order to ensure $\mathcal{C}^1$ continuity at the wall on the sides of the inlet. No-slip conditions are imposed on the walls and homogeneous Neumann on the outlet. The characteristic length of the domain is taken as $L = 0.2$, and the optimal configuration is derived for $\mathrm{Re} = 5$ and $\mathrm{Re} = 150$. The results are then compared to the reference [48] and the plots of volume and objective functional are presented as proof of the correct functioning of the algorithm. The required volume fraction is set to $V_{\mathrm{req}} = 0.08\pi$ in accordance with the reference. This is the portion of the area of a circular annulus needed to connect inlet and outlet, due to the fact that as Re approaches infinity, the optimal configuration asymptotically tends to this shape.

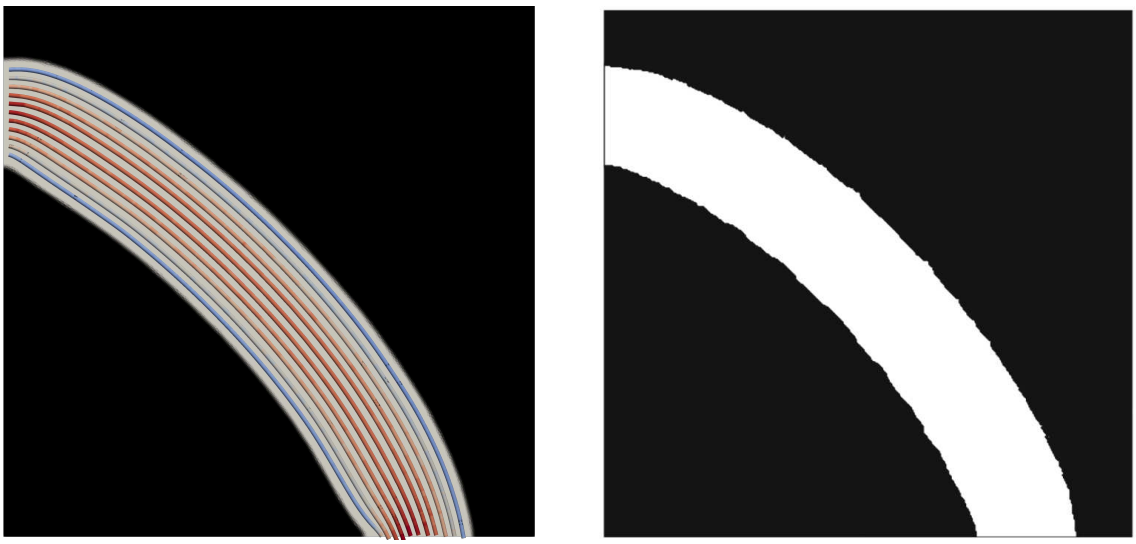

Figure 5.12: Results obtained for Re = 5: the solution from this work on the left with velocity streamlines superimposed, the reference on the right

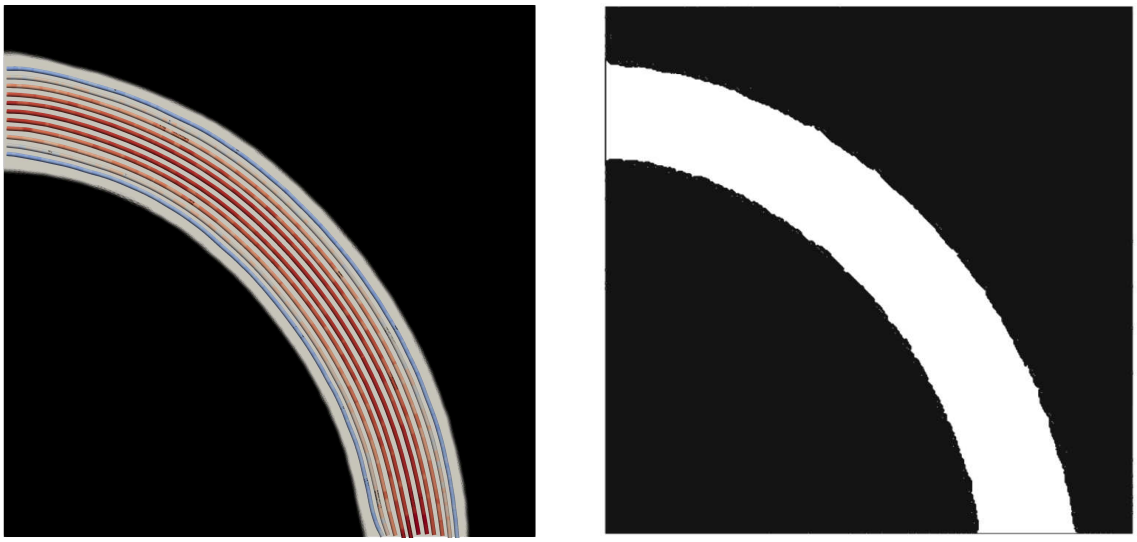

Figure 5.13: Results obtained for Re = 150: the solution from this work on the left with velocity streamlines superimposed, the reference on the right

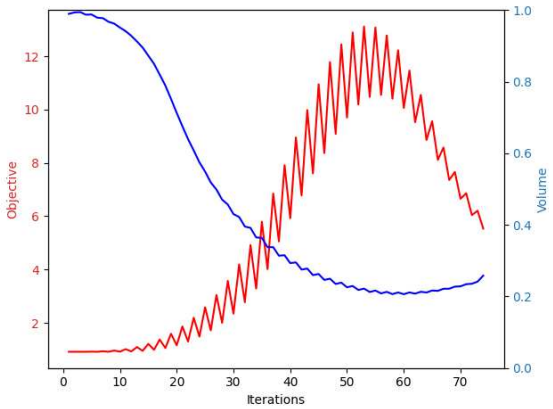

Figure 5.14: Convergence history of the objective functional and the volume constraint, compared for Re=5.

In figure 5.14, the convergence profile of the objective functional is presented together with the same plot for

volume constraint. Two aspects deserve particular attention: the oscillations in the objective functional are due to the way the augmented Lagrangian method for volume. At each iteration a constant fraction of volume is added to the domain. If at iteration i the algorithm creates a duct, at iteration $i+1$ the sensitivity in said duct will be 0 but for the volume constraint, since $\phi \sim 0$ where no volume is present. This causes the observed oscillations, as the parts of the chamber that the algorithm wants to empty of solid at iteration i are filled with a bit of solid at the next, then emptied once again, and so on. This goes on until the required fraction of volume is reached, and in the plot affects the objective functional as shown. In the next section, a tactic to address this issue is proposed. The second behavior that deserves a comment is the fact that the objective functional increases for the majority of the iterations. Once again, this is due to the volume constraint. At the beginning of the algorithm, far from the required fraction of material, the volume constraint dominates the sensitivity and thus leads the objective far from the minimum. When the constraint is satisfied, the sensitivity can prioritize the minimization of the objective and thus the quick downwards turn in the latter iterations is explained.

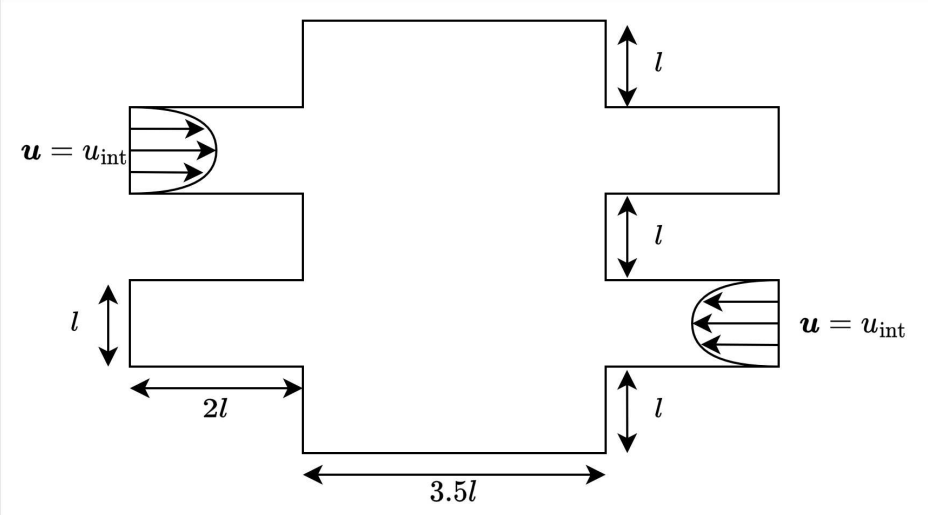

Figure 5.15: Schematics of the test case

In figure 5.15 a schematic representation of the domain and boundary conditions is presented. A parabolic velocity profile is enforced on the inlets, with $\boldsymbol{u}_{max} = 1$. No-slip conditions are imposed on the walls and homogeneous Neumann on the outlets. The characteristic length of the domain is taken as $l = 1$, and the optimal configuration is derived for $\mathrm{Re} = 20$ and $\mathrm{Re} = 200$ and compared to the reference [49]. Plots of volume and objective functional are then presented.

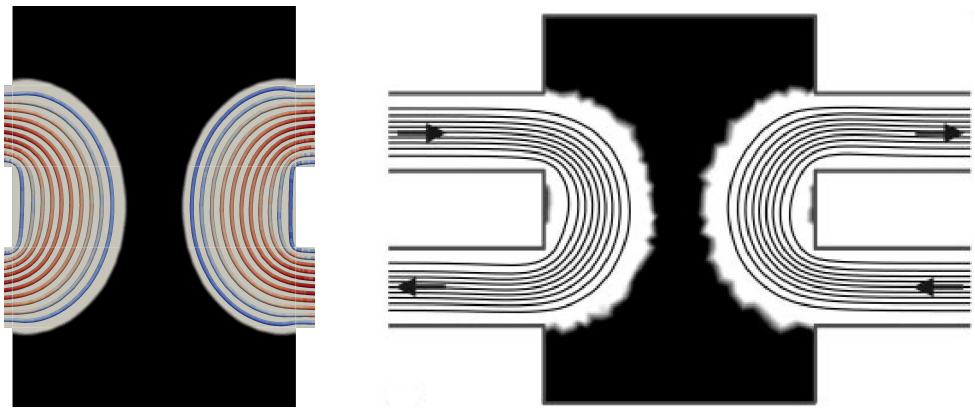

Figure 5.16: Results obtained for $\mathrm{Re} = 20$: the solution from this work on the left, the reference on the right. Velocity streamlines are superimposed to the optimal configuration.

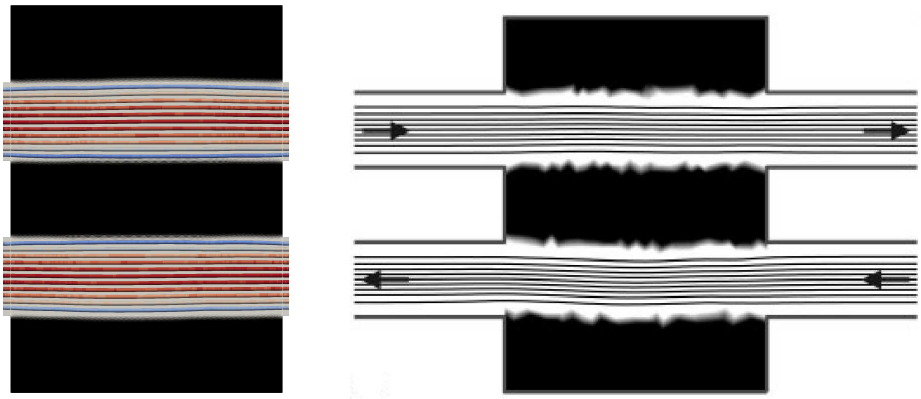

Figure 5.17: Results obtained for Re = 200: the solution from this work on the left, the reference on the right. Velocity streamlines are superimposed to the optimal configuration.

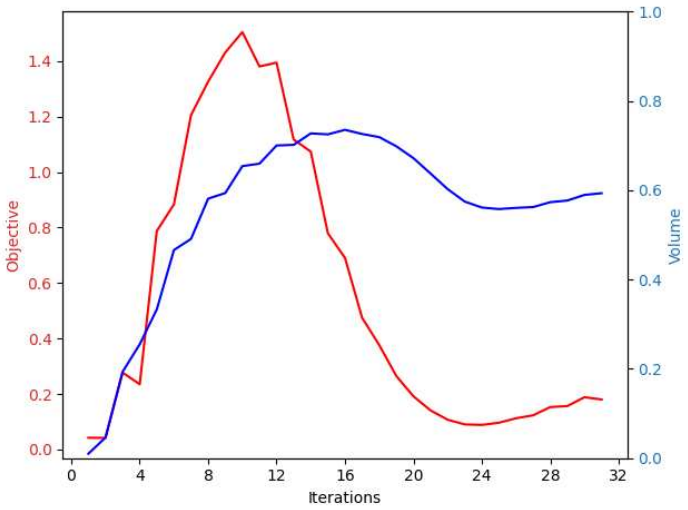

Figure 5.18: Convergence history of the objective functional and volume constraint for Re = 200

Notice in figures 5.16 and 5.17 the higher resolution awarded by the use of adaptive meshing techniques, in comparison with the reference, while maintaining an analogue shape of the ducts. In figure 5.18, the behavior mentioned in the previous section is once again observed. In this case the oscillations are mitigated by a minor modification in the volume constraint. Applying the volume constraint only where the design variable ϕ is greater than a given tolerance, here set at 10^{-4}, is sufficient to speed up convergence and smooth the oscillations observed in the previous case, in plot 5.14. This method should not be used in multi-physics problems, as important information might be erased, depending on the form of the sensitivity.

5.3 Topology optimization of a heat sink with forced convection

The full optimizer involving the solution of the state and adjoint equation for the coupled problem is now presented. For this section the optimization parameters are set to $\alpha_{\max} = 2.5 \cdot 10^4$, $\alpha_{\min} = 2.5 \cdot 10^{-4}$, $\kappa = 10^{-4}$, $\beta_{\max} = 20$. The augmented Lagrangian parameters are set to $\lambda_0 = 0, \gamma = 1.025$. The sensitivity to the parameter z_0 will be studied as a demonstration of the abundance of local minima near the Pareto front, to the point that changing the rate at which the volume is added to the domain can lead to significantly different optimized topologies.

Consider the simple test case of a square chamber with an inlet of size $L = 1$, and side $H = 3L$. Two channels entering and exiting the chamber are added, in order to let the flow fully develop before entering the chamber and before reaching the outlet. The boundary conditions are: fixed velocity $\boldsymbol{u} = (1, 0)$ and temperature $T = 0$ on the inlet, no-slip and adiabatic on walls, and homogeneous Neumann and adiabatic on the outlet. Since characteristic length and velocity are given (both set to 1) Reynolds number is controlled using the viscosity and set to Re = 20 for this section. Prandtl number is set to Pr = 6.7, characteristic value for water. The domain is

represented schematically in figure 5.19. Despite the symmetry of the domain, the equations are solved without exploiting it, simulating the whole domain. All the FEM problems are solved on a structured mesh with 35200 elements, shown in figure 5.20, until the mesh adaptation takes place.

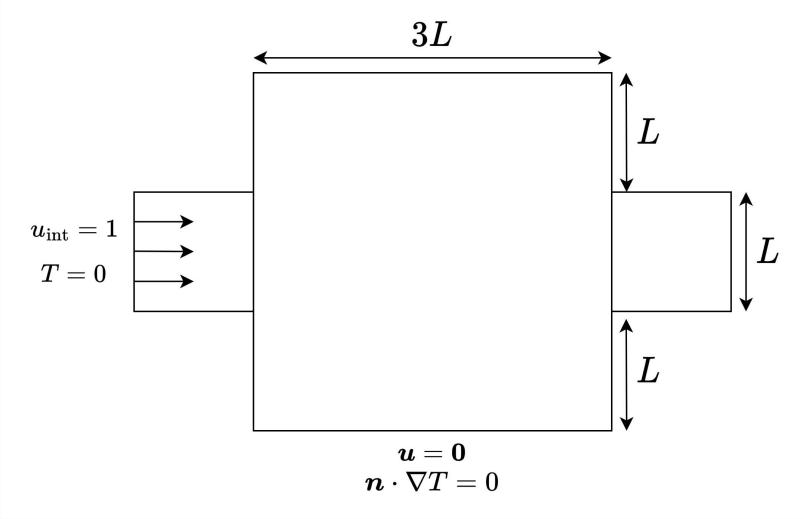

Figure 5.19: Schematic representation of the domain

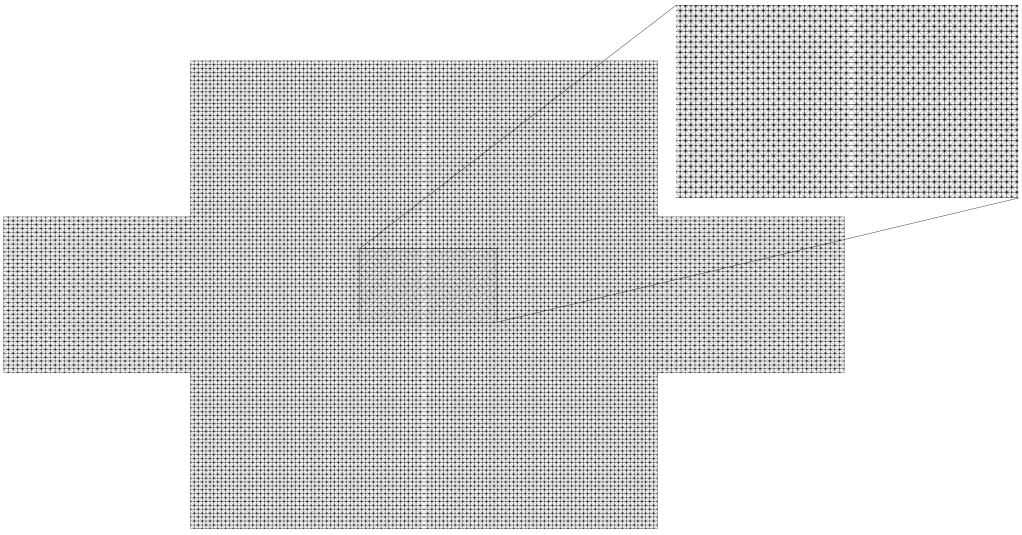

Figure 5.20: Mesh used before the DWP loop

Some optimal configurations are presented as an example of the kind of structures formed, and of the variability that can be introduced varying z_0. This parameter was introduced in section 4.2, and it is a penalization parameter in the volume constraint. More precisely, this parameter can be seen as regulating how aggressively the volume constraint is enforced. In practice, increasing it means increasing the constant fraction of volume added to the domain at each iteration.

(a) $z_0 = 0.01$ (b) $z_0 = 0.1$ (c) $z_0 = 1$

Figure 5.21: Optimal configurations reached for $\nu = 0.65$, varying z_0

With such an abundance of local minima, changing the other parameters not strictly bound to the physics, like $\alpha_{\max}$ and $\beta_{\max}$, has a relevant influence on the results. The influence of β has been explored in studies [12] and [30], among others, and it has been revealed that the geometrical complexity of the structures produced increases with this parameter. The same can be said for the stabilization parameter κ, with the same study [12] as a reference.

It is not suggested, however, to change $\alpha_{\max}$, as increasing/decreasing the porosity of the solid material can allow/block more of the fluid, thus changing the refrigeration provided and significantly affecting the objective functional as a result. This makes the comparison between geometries obtained with different values of $\alpha_{\max}$ challenging at the very least.

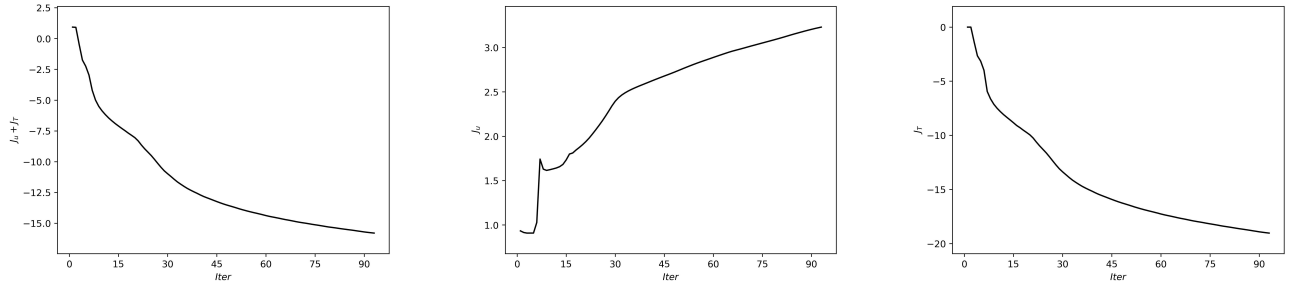

(a) $\nu J_T + (1-\nu)J_{\boldsymbol{u}}$ (b) $(1-\nu)J_{\boldsymbol{u}}$ (c) νJ_T

Figure 5.22: Convergence profiles of the various objective functionals for the case $\nu = 0.65$, $z_0 = 0.01$.

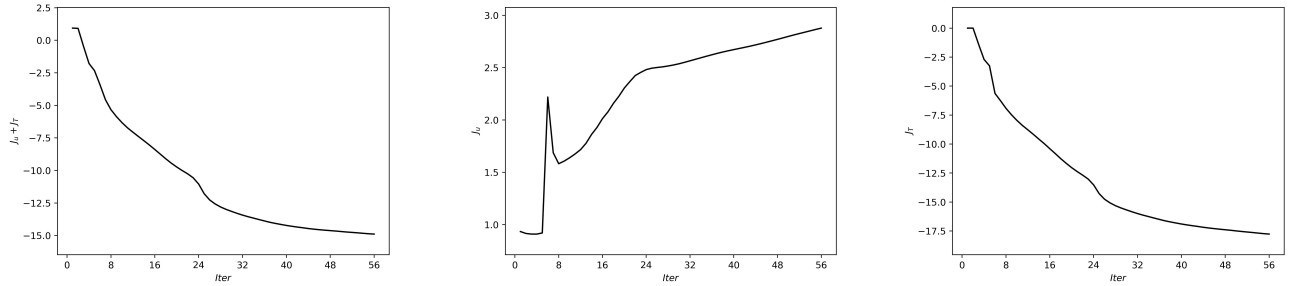

(a) $\nu J_T + (1-\nu)J_{\boldsymbol{u}}$ (b) $(1-\nu)J_{\boldsymbol{u}}$ (c) νJ_T

Figure 5.23: Convergence profiles of the various objective functionals for the case $\nu = 0.65$, $z_0 = 0.1$.

In figures 5.22 and 5.23 the convergence history for the objective functionals are presented together with their combination, that represents the actual objective as the algorithm sees it. Notice that differently from the single-objective minimization shown in the previous section, no oscillations are observed in the objective functional.

Another aspect that deserves attention is the speed of convergence. Comparing the convergence histories shown in figures 5.22, 5.23 the difference is striking. Increasing z_0 by one order of magnitude, the iterations required for convergence are decreased by a factor 2. The trade-off is in complexity of the structures generated inside the domain. In this way z_0 has an impact similar to the stabilization coefficient κ, whose influence on the result has been studied in [12] and [11], among others.
When dealing with a problem with competitive objective functionals, such as the problem at hand, increasing one means decreasing the other. The set of all optimal solution in the space $(J_{\boldsymbol{u}}, J_T)$ is called Pareto frontier. This means that travelling along the frontier, all the solution that make the most out of the exchange between the two functionals are met. A proper exploration of the Pareto frontier would require a more sophisticated algorithm, such as the one employed in [27], but here the computed approximation of the frontier can serve as a confirmation of the shifting balance between the two opposing objective functionals. The simulation is run to convergence for 30 cases: the weight is varied as $\nu = 0.05 + 0.1i$, with $i \in \mathcal{N} = 0, 1, 2..., 9$. For each value of ν the solution is computed for $z_0 = 1, 0.1, 0.01$.

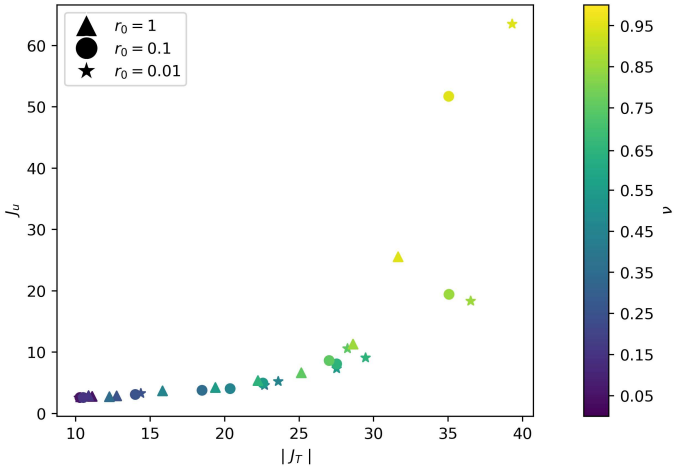

Figure 5.24: Approximation of the Pareto frontier given by the weighted sum method. The color map represents different values of the weight ν.

Notice in figure 5.24 how the weighted sum method fails to capture a portion of the Pareto frontier, as going in the direction $J_T > 0$ there is a progressive shortness of points despite changing the weight coefficients with even spacing. This is consistent with the results obtained by [27], where the weighted sum method shows the same inability to approximate the same section of the optimization front. The other points, however, seem clustered to form the typical convex shape of the Pareto frontier. Still, study [27], shows that with the use of algorithms sophisticated enough to allow the escape from the local minima, even better, cleaner approximation of the front can be obtained, and thus better performing optimal configurations. Towards the lower left part of the front, approaching the origin, the algorithm shows a much higher capability to approximate the frontier, as the thermal functional loses importance and the problem becomes more convex thanks to the pressure drop objective functional.

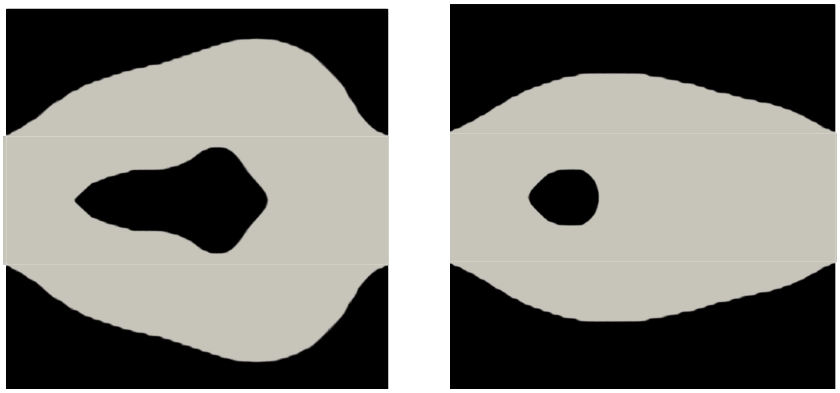

(a) $\nu = 0.45$, $z_0 = 0.1$

(b) $\nu = 0.45$, $z_0 = 1$

(c) $\nu = 0.85$, $z_0 = 0.01$

(d) $\nu = 0.85$, $z_0 = 0.1$

Figure 5.25: Some of the Pareto optimal configuration reached varying the weight ν and the initial volume penalization z_0. The configurations obtained for $\nu = 0.85$ perform far above the configurations obtained with similar parameters, suggesting a good approximation of the Pareto front.

In figure 5.25 some more obtained geometries are presented. Comparing the results leads to some observations:

- The algorithm often prefers to split the flow as soon as possible: this is coherent with the last term of the energy equation (2.4), that ensures that wherever solid material lies, heat is produced.
- Splittings in the flow and the creation of smaller channels are beneficial to heat dissipation but require a higher total pressure drop to effectively pump the fluid through.
- It appears important for low ν to fill the sides of the chamber with solid, probably to minimize pressure losses due to residual velocity in the solid domain. For high ν the algorithm often gives less importance to filling the corners.
- Raising the value of z_0 usually leads to more compact structures and less fragmented bodies in the channel. When ν is high this leads to designs that favor pressure drop reduction over heat exchange, compared to those obtained with the same value of ν.

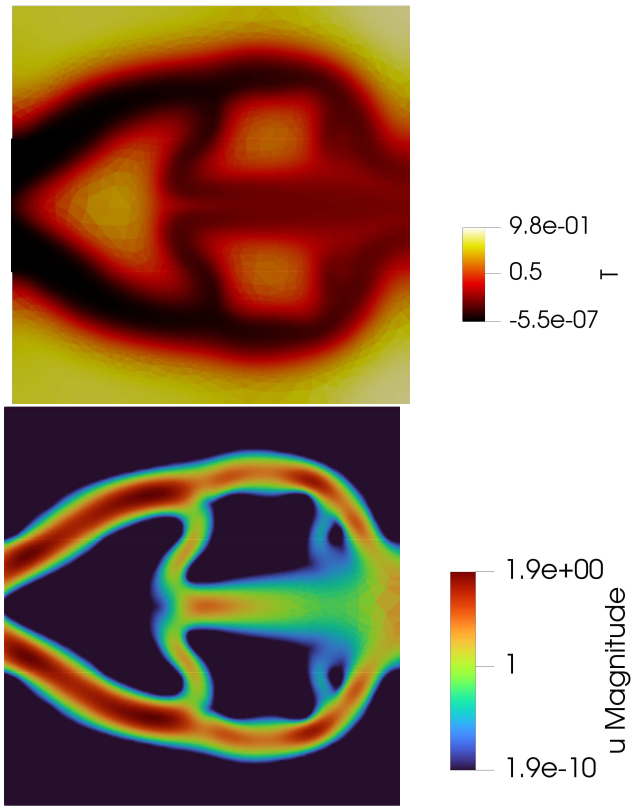

Figure 5.26: Dimensionless temperature and velocity field in the final configuration for case 5.25d.

Velocity magnitude and temperature field in the Pareto optimal configurations have been plotted in order to check that no abnormalities are present.
The case shown as an example in figure 5.26 is the one presented in figure 5.25d.

Chapter 6

Conclusions

This academic work encompasses the presentation and extension of the steady incompressible Conjugate Heat Transfer (CHT) problem within a framework that models interaction with the solid domain. A coupled non-linear solver has been developed and tested, and then integrated into a topology optimization pipeline. The overarching goal has been to generate optimized heat sink geometries for a specified test case.
Within this context, the adjoint method for topology optimization is introduced and tailored to address the specific intricacies of the problem at hand, with a comprehensive explanation of the computational procedures. Utilizing the Finite Element Method, both primal and adjoint variables are computed, enabling the determination of sensitivity through the same method.

The challenges encountered during algorithm development are presented, and post-processing techniques such as mesh adaptation and the Double Well Potential are proposed as viable options for resolving these challenges. The multi-objective optimization problem has been modeled using the weighted sum method. This method's main advantage is its striking simplicity in the implementation, but as shown in the last section the drawback is its limited capability to explore the Pareto front, given its tendency to get stuck in local minima. This weakness however does not prevent the algorithm from producing efficient geometries, and the general sensitivity to parameters allows to fine-tune the algorithm to the desired application. Adding that generally the local minima are close to each other in terms of final performance, but not in terms of shape of the internal structures, the variability in the results can be seen as an advantage.

Another limitation the algorithm can be somewhat tuned around is the number of iterations needed for convergence, as higher values of z_0 generally necessitate fewer iterations, but paying the price in complexity of the resulting structures.

6.1 Further developments

Regarding future continuations of this work, treatment of the volume constraint and the volume initialization are in need of an in-depth analysis, as they often work to penalize some configurations with respect to others, as observed by [49].

The natural evolution of this work is the integration in a proper Pareto frontier approximation setting. This requires extending the algorithm to make it capable of exploring around the local minima: one intuitive way to do so are adaptive weighting schemes [27], since they can be seen as an improvement on the regular weighted sum method.

The approach presented in this paper can also be seen as a base-line for multi-fidelity simulations in the context of industrial applications. The size of the simulations needed by the industry, and the need to solve multiple set of PDEs at each iteration imply that running the algorithm on a full scale case, possibly in 3D, is at the moment unfeasible. However, approaches like [50] suggest that surrogate model may play an important role in the future of this subject.

Bibliography

[1] Grégoire Allaire, editor. *Conception optimale de structures*. SpringerLink. Springer Berlin Heidelberg, Berlin, Heidelberg, 2007. Includes bibliographical references and index.

[2] William Prager. A note on discretized michell structures. *Computer Methods in Applied Mechanics and Engineering*, 3(3):349–355, May 1974.

[3] Krister Svanberg. Optimization of geometry in truss design. *Computer Methods in Applied Mechanics and Engineering*, 28(1):63–80, August 1981.

[4] Olivier Pironneau. *Optimal Shape Design for Elliptic Systems*. Springer Berlin Heidelberg, 1984.

[5] Jan Sokolowski and Jean-Paul Zolesio. *Introduction to Shape Optimization*. Springer Berlin Heidelberg, 1992.

[6] Martin Philip Bendsøe and Noboru Kikuchi. Generating optimal topologies in structural design using a homogenization method. *Computer Methods in Applied Mechanics and Engineering*, 71(2):197–224, November 1988.

[7] Martin P. Bendsøe and Ole Sigmund. *Topology Optimization*. Springer Berlin Heidelberg, 2004.

[8] Pedro Gomes and Rafael Palacios. Aerodynamic-driven topology optimization of compliant airfoils. *Structural and Multidisciplinary Optimization*, 62(4):2117–2130, May 2020.

[9] Rodrigo L. Pereira, Heitor N. Lopes, and Renato Pavanello. Topology optimization of acoustic systems with a multiconstrained beso approach. *Finite Elements in Analysis and Design*, 201:103701, April 2022.

[10] Naoki Kishimoto, Kazuhiro Izui, Shinji Nishiwaki, and Takayuki Yamada. Optimal design of electromagnetic cloaks with multiple dielectric materials by topology optimization. *Applied Physics Letters*, 110(20), May 2017.

[11] Takayuki Yamada, Kazuhiro Izui, Shinji Nishiwaki, and Akihiro Takezawa. A topology optimization method based on the level set method incorporating a fictitious interface energy. *Computer Methods in Applied Mechanics and Engineering*, 199(45–48):2876–2891, November 2010.

[12] Kentaro Yaji, Takayuki Yamada, Seiji Kubo, Kazuhiro Izui, and Shinji Nishiwaki. A topology optimization method for a coupled thermal–fluid problem using level set boundary expressions. *International Journal of Heat and Mass Transfer*, 81:878–888, 2015.

[13] Martin Philip Bendsøe and Noboru Kikuchi. Generating optimal topologies in structural design using a homogenization method. *Computer Methods in Applied Mechanics and Engineering*, 71(2):197–224, November 1988.

[14] Ole Sigmund. Morphology-based black and white filters for topology optimization. *Structural and Multidisciplinary Optimization*, 33(4–5):401–424, January 2007.

[15] Ole Sigmund and Kurt Maute. Topology optimization approaches: A comparative review. *Structural and Multidisciplinary Optimization*, 48(6):1031–1055, August 2013.

[16] Daniel Hartmann, Matthias Meinke, and Wolfgang Schröder. The constrained reinitialization equation for level set methods. *Journal of Computational Physics*, 229(5):1514–1535, March 2010.

[17] Arun L. Gain and Glaucio H. Paulino. A critical comparative assessment of differential equation-driven methods for structural topology optimization. *Structural and Multidisciplinary Optimization*, 48(4):685–710, July 2013.

[18] Akihiro Takezawa, Shinji Nishiwaki, and Mitsuru Kitamura. Shape and topology optimization based on the phase field method and sensitivity analysis. *Journal of Computational Physics*, 229(7):2697–2718, April 2010.

[19] Shiwei Zhou and Michael Yu Wang. Multimaterial structural topology optimization with a generalized cahn–hilliard model of multiphase transition. *Structural and Multidisciplinary Optimization*, 33(2):89–111, July 2006.

[20] Hong Kyoung Seong, Hyundo Shin, Jeonghoon Yoo, Takayuki Yamada, and Shinji Nishiwaki. Reaction-diffusion equation based topology optimization combined with the modified conjugate gradient method. *Finite Elements in Analysis and Design*, 140:84–95, February 2018.

[21] Pontrâgin Lev Semënovič, Boltyanski Vladimir Grigorevich, Gamkrelidze Revaz Valerianovich, Mishchenko Evgenii Frolovich, Brown D. E., and Lev Semënovič Pontrâgin. *The mathematical theory of optimal processes / L. S. Pontryagin, V. G. Boltyanskii, R. V. Gamkrelidze, E.F. Mishchenko ; translated by D. E. Brown.* International series of monographs in pure and applied mathematics. Pergamon Press The MacMillan Comany, Oxford Paris [etc.] New York, 1964.

[22] Jacques-Louis Lions. *Optimal control of systems governed by partial differential equations.* Number 170 in Die @Grundlehren der mathematischen Wissenschaften in Einzeldarstellungen. Springer, Berlin, 1971.

[23] Thomas Borrvall and Joakim Petersson. Topology optimization of fluids in stokes flow. *International Journal for Numerical Methods in Fluids*, 41(1):77–107, December 2002.

[24] A. Gersborg-Hansen, O. Sigmund, and R.B. Haber. Topology optimization of channel flow problems. *Structural and Multidisciplinary Optimization*, 30(3):181–192, June 2005.

[25] Shiwei Zhou and Qing Li. A variational level set method for the topology optimization of steady-state navier–stokes flow. *Journal of Computational Physics*, 227(24):10178–10195, December 2008.

[26] Yongbo Deng, Zhenyu Liu, and Yihui Wu. Topology optimization of steady and unsteady incompressible navier–stokes flows driven by body forces. *Structural and Multidisciplinary Optimization*, 47(4):555–570, November 2012.

[27] Yuki Sato, Kentaro Yaji, Kazuhiro Izui, Takayuki Yamada, and Shinji Nishiwaki. An optimum design method for a thermal-fluid device incorporating multiobjective topology optimization with an adaptive weighting scheme. *Journal of Mechanical Design*, 140(3), 2018.

[28] Ercan M. Dede. Optimization and design of a multipass branching microchannel heat sink for electronics cooling. *Journal of Electronic Packaging*, 134(4), August 2012.

[29] Adriano Akio Koga, Edson Comini C Lopes, Helcio F. Villa Nova, Cícero Ribeiro de Lima, and Emílio Carlos Nelli Silva. Development of heat sink device by using topology optimization. *International Journal of Heat and Mass Transfer*, 2013.

[30] Tadayoshi Matsumori, Tsuguo Kondoh, Atsushi Kawamoto, and Tsuyoshi Nomura. Topology optimization for fluid–thermal interaction problems under constant input power. *Structural and Multidisciplinary Optimization*, 47(4):571–581, February 2013.

[31] Juhani Koski. *Multicriteria Truss Optimization*, pages 263–307. Springer US, 1988.

[32] On a bicriterion formulation of the problems of integrated system identification and system optimization. *IEEE Transactions on Systems, Man, and Cybernetics*, SMC-1(3):296–297, 1971.

[33] Indraneel Das and J. E. Dennis. Normal-boundary intersection: A new method for generating the pareto surface in nonlinear multicriteria optimization problems. *SIAM Journal on Optimization*, 8(3):631–657, August 1998.

[34]

[35] Heeseung Lim, Jeonghoon Yoo, and Jae Seok Choi. Topological nano-aperture configuration by structural optimization based on the phase field method. *Structural and Multidisciplinary Optimization*, 49(2):209–224, July 2013.

[36] Jae Seok Choi, Takayuki Yamada, Kazuhiro Izui, Shinji Nishiwaki, and Jeonghoon Yoo. Topology optimization using a reaction–diffusion equation. *Computer Methods in Applied Mechanics and Engineering*, 200(29–32):2407–2420, July 2011.

[37] F. Hecht. New development in freefem++. *Journal of Numerical Mathematics*, 20(3–4), January 2012.

[38] Jean Donea and Antonio Huerta. *Finite element methods for flow problems.* Wiley, 2004.

[39] M. P. Bendsøe and O. Sigmund. Material interpolation schemes in topology optimization. *Archive of Applied Mechanics (Ingenieur Archiv)*, 69(9–10):635–654, November 1999.

[40] Richard P. Dwight and Joel Brezillon. Effect of approximations of the discrete adjoint on gradient-based optimization. *AIAA Journal*, 44(12):3022–3031, December 2006.

[41] C. Othmer. A continuous adjoint formulation for the computation of topological and surface sensitivities of ducted flows. *International Journal for Numerical Methods in Fluids*, 58(8):861–877, 2008.

[42] Gilles Marck, Maroun Nemer, and Jean-Luc Harion. Topology optimization of heat and mass transfer problems: Laminar flow. *Numerical Heat Transfer, Part B: Fundamentals*, 63(6):508–539, June 2013.

[43] Cheolwoong Kim, Mingook Jung, Takayuki Yamada, Shinji Nishiwaki, and Jeonghoon Yoo. Freefem++ code for reaction-diffusion equation–based topology optimization: for high-resolution boundary representation using adaptive mesh refinement. *Structural and Multidisciplinary Optimization*, 62(1):439–455, February 2020.

[44] Dimitri P. Bertsekas. *Constrained optimization and Lagrange multiplier methods*. Number 4 in Athena scientific optimization and computation series. Athena Scientific, Belmont, Mass., 1996.

[45] Daniel Rolando Araya Matilla. Enhancing topology optimisation of elastic structures via mesh adaptation. Master's thesis, Universitat Politècnica de Catalunya, 2023.

[46] U Ghia, K.N Ghia, and C.T Shin. High-re solutions for incompressible flow using the navier-stokes equations and a multigrid method. *Journal of Computational Physics*, 48(3):387–411, December 1982.

[47] Dipankar Chatterjee and Bittagopal Mondal. Effect of thermal buoyancy on vortex shedding behind a square cylinder in cross flow at low reynolds numbers. *International Journal of Heat and Mass Transfer*, 54(25–26):5262–5274, 2011.

[48] Xiaoxia Dai, Chengwei Zhang, Ye Zhang, and Mårten Gulliksson. Topology optimization of steady navier-stokes flow via a piecewise constant level set method. *Structural and Multidisciplinary Optimization*, 57(6):2193–2203, November 2017.

[49] Laurits Højgaard Olesen, Fridolin Okkels, and Henrik Bruus. A high-level programming-language implementation of topology optimization applied to steady-state navier–stokes flow. *International Journal for Numerical Methods in Engineering*, 65(7):975–1001, 2005.

[50] Xi Zhao, Mingdong Zhou, Ole Sigmund, and Casper Schousboe Andreasen. A "poor man's approach" to topology optimization of cooling channels based on a darcy flow model. *International Journal of Heat and Mass Transfer*, 116:1108–1123, January 2018.

[51] O. C. Zienkiewicz and J. Z. Zhu. The superconvergent patch recovery and a posteriori error estimates. part 1: The recovery technique. *International Journal for Numerical Methods in Engineering*, 33(7):1331–1364, May 1992.

[52] O. C. Zienkiewicz and J. Z. Zhu. The superconvergent patch recovery and a posteriori error estimates. part 2: Error estimates and adaptivity. *International Journal for Numerical Methods in Engineering*, 33(7):1365–1382, May 1992.

[53] S. Micheletti and S. Perotto. *Anisotropic Adaptation via a Zienkiewicz–Zhu Error Estimator for 2D Elliptic Problems*, pages 645–653. Springer Berlin Heidelberg, 2010.

[54] G. M. Porta, S. Perotto, and F. Ballio. Anisotropic mesh adaptation driven by a recovery-based error estimator for shallow water flow modeling. *International Journal for Numerical Methods in Fluids*, 70(3):269–299, September 2011.

Chapter 7

Appendix

7.1 Appendix A: Equivalence between pressure drop and total potential energy

This section follows closely the similar derivation from [27]. Consider the extended incompressible steady-state Navier-Stokes equation, presented in equation (2.4), multiply by the velocity $\boldsymbol{u}$ and integrate it over the domain Ω. The result is

$$\begin{aligned}&\int_\Omega (\boldsymbol{u}\cdot\nabla)\boldsymbol{u}\cdot\boldsymbol{u}d\Omega+\int_\Omega \nabla p\cdot\boldsymbol{u}d\Omega\\&-\int_\Omega \frac{1}{\mathrm{Re}}\nabla^2\boldsymbol{u}\cdot\boldsymbol{u}d\Omega+\int_\Omega \alpha(\phi)\,\boldsymbol{u}\cdot\boldsymbol{u}d\Omega=0.\end{aligned}$$

Integrating by parts and using the incompressibility condition $\nabla\cdot\boldsymbol{u}=0$ yields

$$\begin{aligned}&\int_\Gamma \frac{1}{2}(\boldsymbol{u}\cdot\boldsymbol{u})\boldsymbol{u}\cdot\boldsymbol{n}d\Gamma+\int_\Gamma p\boldsymbol{u}\cdot\boldsymbol{n}d\Gamma\\&-\int_\Gamma \frac{1}{\mathrm{Re}}\boldsymbol{n}\cdot\nabla\boldsymbol{u}\boldsymbol{u}d\Gamma\\&+\int_\Omega \frac{1}{\mathrm{Re}}\nabla\boldsymbol{u}:\nabla\boldsymbol{u}d\Omega+\int_\Omega \alpha(\phi)\,\boldsymbol{u}\cdot\boldsymbol{u}d\Omega=0,\end{aligned}$$

Now, using that $\boldsymbol{u}=0$ on Γ_{wall} , the equation becomes

$$\begin{aligned}&\int_{\Gamma_{\text{in}}\cup\Gamma_{\text{out}}} \left(p+\frac{1}{2}|\boldsymbol{u}|^2\right)(\boldsymbol{u}\cdot\boldsymbol{n})d\Gamma\\&-\int_{\Gamma_{\text{in}}\cup\Gamma_{\text{out}}} \frac{1}{\mathrm{Re}}\boldsymbol{n}\cdot\nabla\boldsymbol{u}\boldsymbol{u}d\Gamma\\&+\int_\Omega \frac{1}{\mathrm{Re}}\nabla\boldsymbol{u}:\nabla\boldsymbol{u}d\Omega+\int_\Omega \alpha(\phi)\,\boldsymbol{u}\cdot\boldsymbol{u}d\Omega=0.\end{aligned}$$

Notice that the second term of this equation vanishes the flow on $\Gamma_{\text{in}}\cup\Gamma_{\text{out}}$ fully developed, i.e. when $\boldsymbol{u}=U\boldsymbol{n}$, and therefore

$$\begin{aligned}&\int_{\Gamma_{\text{in}}\cup\Gamma_{\text{out}}} \frac{1}{\mathrm{Re}}U\boldsymbol{n}\left(\nabla\boldsymbol{u}\boldsymbol{u}\right)d\Gamma\\&=\int_{\Gamma_{\text{in}}\cup\Gamma_{\text{out}}} \frac{1}{\mathrm{Re}}U\boldsymbol{n}\otimes\boldsymbol{n}:\nabla\boldsymbol{u}d\Gamma=0.\end{aligned}$$

Finally, everything is rewritten as

$$\begin{aligned}&\int_\Omega \left(\frac{1}{\mathrm{Re}}\nabla\boldsymbol{u}:\nabla\boldsymbol{u}+\alpha(\phi)\,\boldsymbol{u}\cdot\boldsymbol{u}\right)d\Omega\\&=\int_{\Gamma_{\text{in}}\cup\Gamma_{\text{out}}} \left(p+\frac{1}{2}|\boldsymbol{u}|^2\right)(-\boldsymbol{u}\cdot\boldsymbol{n})d\Gamma\end{aligned}$$

This means that the total potential energy is equivalent to the total pressure drop for incompressible fluids.

7.2 Appendix B: Newton-Raphson algorithm for Navier-Stokes equations

A non linear solver is needed for the solution of the linear system arising from the discretization of the Navier-Stokes equation. In this subsection the method is briefly presented and specialized to the solution of this system. The reasons that lead to the choice of this solution method are robustness and accuracy. Here the fact that the systems of equations maintain a sizeable dimension is exploited, allowing for such an expensive method.
A Newton-Raphson iteration for vector-valued functions can be formulated as

$$\mathrm{x}^{k+1} = \mathrm{x}^k + \delta_{\mathrm{x}}^k$$

where

$$\delta_{\mathbf{x}}^k = -\left(\nabla F\left(\mathrm{x}^k\right)\right)^{-1} F\left(\mathrm{x}^k\right)$$

$\nabla F\left(\mathrm{x}^k\right)$ denotes the Jacobian of $F(\mathrm{x})$ evaluated at x^k. Now recast the Navier-Stokes problem in strong form as: find $(\boldsymbol{u}, p)$ such that

$$F(\boldsymbol{u}, p) = \begin{pmatrix} -\frac{1}{\mathrm{Re}}\triangle\boldsymbol{u} + (\boldsymbol{u}\cdot\nabla)\boldsymbol{u} + \nabla p - \mathbf{f} \\ -\nabla\cdot\boldsymbol{u} \end{pmatrix} = \begin{pmatrix} 0 \\ 0 \end{pmatrix}$$

The definition of the Newton correction can be rearranged as

$$\nabla F\left(\mathrm{x}^k\right)\delta_{\mathrm{x}}^k = -F\left(\mathrm{x}^k\right)$$

Now,

- The left-hand side represents the directional gradient, so it can be rewritten using the basic definition

$$\begin{aligned} &\nabla F\left(\mathbf{x}^k\right)\delta_{\mathbf{x}}^k = \nabla F\left(\boldsymbol{u}^k, p\right)\left(\delta_{\boldsymbol{u}}^k, \delta_p^k\right) \\ &= \lim_{\epsilon\to 0}\frac{1}{\epsilon}\left(F\left(\boldsymbol{u}^k + \epsilon\delta_{\boldsymbol{u}}^k, p^k + \epsilon\nabla\delta_p^k\right) - \left(F\left(\boldsymbol{u}^k, p^k\right)\right)\right. \end{aligned}$$

$$\begin{aligned} &= \lim_{\epsilon\to 0}\frac{1}{\epsilon}\begin{pmatrix} -\epsilon\frac{1}{\mathrm{Re}}\Delta\delta_{\boldsymbol{u}}^k + \epsilon\boldsymbol{u}^k\cdot\nabla\delta_{\boldsymbol{u}}^k + \epsilon\delta_{\boldsymbol{u}}^k\cdot\nabla\boldsymbol{u}^k + \epsilon^2\delta_{\boldsymbol{u}}^k\cdot\nabla\delta_{\boldsymbol{u}}^k + \epsilon\nabla\delta_p^k \\ -\epsilon\nabla\cdot\delta_{\boldsymbol{u}}^k \end{pmatrix} \\ &= \begin{pmatrix} -\frac{1}{\mathrm{Re}}\Delta\delta_{\boldsymbol{u}}^k + \boldsymbol{u}^k\cdot\nabla\delta_{\boldsymbol{u}}^k + \delta_{\boldsymbol{u}}^k\cdot\nabla\boldsymbol{u}^k + \nabla\delta_p^k \\ -\nabla\cdot\delta_{\boldsymbol{u}}^k \end{pmatrix}. \end{aligned}$$

- And the right-hand side is

$$-F\left(\mathbf{x}^k\right) = -F\left(\boldsymbol{u}^k, p^k\right) = \begin{pmatrix} \mathbf{f} + \frac{1}{\mathrm{Re}}\Delta\boldsymbol{u}^k - \boldsymbol{u}^k\cdot\nabla\boldsymbol{u}^k - \nabla p^k \\ \nabla\cdot\boldsymbol{u}^k \end{pmatrix}.$$

  Calling $\overline{\mathbf{f}}^k = \mathbf{f} + \frac{1}{\mathrm{Re}}\Delta\boldsymbol{u}^k - \boldsymbol{u}^k\cdot\nabla\boldsymbol{u}^k - \nabla p^k$, obtain the equations

$$\begin{cases} -\frac{1}{\mathrm{Re}}\Delta\delta_{\boldsymbol{u}}^k + \boldsymbol{u}^k\cdot\nabla\delta_{\boldsymbol{u}}^k + \delta_{\boldsymbol{u}}^k\cdot\nabla\boldsymbol{u}^k + \nabla\delta_p^k = \overline{\mathbf{f}}^k \\ \nabla\cdot\delta_{\boldsymbol{u}}^k = -\nabla\cdot\boldsymbol{u}^k \end{cases}$$

where $\boldsymbol{u}^k$ and p^k are the solutions from the previous iteration. This is a system with the update term $\delta_{\boldsymbol{u}}^k$ and δ_p^k as the only unknowns, and it is therefore possible to use the Galerkin method once again: multiply by a test function, use stokes theorem, and discretize.
The problem is not yet well posed as the choice on boundary conditions is needed. If a Neumann condition is to be enforced, then no further work is needed. Given Dirichlet boundary conditions, enforce the boundary value on the initial guess and then homogeneous Dirichelet on the corresponding part of the boundary at each iteration of the algorithm.
Schematically:

$$\begin{aligned} \boldsymbol{u}^0\big|_{\Gamma_D} &= \boldsymbol{u}_D \\ \delta_{\boldsymbol{u}}^k\Big|_{\Gamma_D} &= \mathbf{0} \text{ for } k > 0, \end{aligned}$$

in order to guarantee $\boldsymbol{u}^{k+1}\big|_{\Gamma_D} = \mathbf{g}$ always holds following $\boldsymbol{u}^{k+1} = \boldsymbol{u}^k + \delta_{\boldsymbol{u}}^k$.

The weak formulation of the problem is then: find $\delta_{\boldsymbol{u}}^k \in \mathcal{S}_0$ (same space with homogeneous Dirichelet BCs) and $\delta_u^k \in \mathcal{Q}$, such that

$$\begin{cases} a(\delta_{\boldsymbol{u}}^k, \boldsymbol{v}) + d(\delta_{\boldsymbol{u}}^k, \boldsymbol{v}) + b(\boldsymbol{v}, \delta_p^k) = (\bar{\mathbf{f}}^k, \boldsymbol{v}) + (\boldsymbol{\tau}, \boldsymbol{v})_{\Gamma_N} & \forall \boldsymbol{v} \in \mathcal{V}, \\ b(\delta_{\boldsymbol{u}}^k, q) = 0 & \forall q \in \mathcal{Q}, \end{cases}$$

where each term has been defined in the previous section, except for the functional

$$d(\delta_{\boldsymbol{u}}^k, \boldsymbol{v}) = \left(\boldsymbol{u}^k \cdot \nabla \delta_{\boldsymbol{u}}^k, \boldsymbol{v}\right) + \left(\delta_{\boldsymbol{u}}^k \cdot \nabla \boldsymbol{u}^k, \boldsymbol{v}\right)$$

with $\boldsymbol{u}^k$ solution computed from the previous iteration. Introducing the usual discrete spaces, and subbing in the discrete counterpart of the terms seen so far, the resulting Galerkin problem is

$$\begin{cases} a(\delta_{\boldsymbol{u}_h}^k, \boldsymbol{v}_h) + d(\delta_{\boldsymbol{u}_h}^k, \boldsymbol{v}_h) + b(\boldsymbol{v}_h, \delta_{p_h}^k) = (\bar{\mathbf{f}}^k, \boldsymbol{v}_h) + (\boldsymbol{\tau}, \boldsymbol{v}_h)_{\Gamma_N} & \forall \boldsymbol{v}_h \in \mathcal{V}^h, \\ b(\delta_{\boldsymbol{u}_h}^k, q) = 0 & \forall q \in \mathcal{Q}^h, \end{cases}$$

which translates to the linear system

$$\begin{pmatrix} \mathbf{K}+\mathbf{D} & \mathbf{G} \\ \mathbf{G}^T & \mathbf{0} \end{pmatrix} \begin{pmatrix} \delta_{\boldsymbol{u}_h}^k \\ \delta_{p_h}^k \end{pmatrix} = \begin{pmatrix} \bar{\mathbf{f}}^k \\ -\nabla \cdot \boldsymbol{u}^k \end{pmatrix}$$

where the solution vector on the left-hand side refers to the values of the correction in the nodes, while each entry of the vector on the right is the result of the integral of the shape functions times the 'forcing' term, which, remember, is the oriented residual of the previous solution.

This is now a linear system, solvable with standard iterative or direct methods.

7.3 Appendix C: Anisotropic mesh adaptation

In this Appendix, a more in depth look to the mesh adaptation algorithm is presented. The implementation used in this work has been developed by [45].
The stretching for each point of the domain is encoded in a function $\mathrm{M} : \mathbb{R}^2 \to \mathbb{R}^{2\times 2}$ called metrics. the computation of the metrics is based on the a posteriori error estimate method proposed by Zienkiewicz and Zhu in [51] and [52]. The idea is to define a reconstruction operator $P(\nabla\phi^h)$ which attempts to improve the approximation offered by the Finite Elements Method, since the gradient of the solution ϕ has worse accuracy of the solution itself. Then an a-posteriori error estimator can be defined from the difference $||p(\nabla\phi^h) - \nabla\phi^h||_{L^2(\Omega)}$. Once again there are multiple choices for the recovery operator such as averages and projections of the numerical gradient $\nabla\phi^h$, but the one considered in this work is the one proposed in [53], hereafter denoted by $\boldsymbol{P}^r_{\Delta_K}\left(\nabla\phi^h\right)$. This is an approximation which has degree r over the patch $\Delta_K = \{T \in \mathcal{T}_h \mid T \cup K \neq \emptyset\}$. The objective is seeking $\boldsymbol{P}^r_{\Delta_K}\left(\nabla\phi^h\right) \in \left[\mathbb{P}_r\left(\Delta_K\right)\right]^2$ such that

$$\int_{\Delta_K} \left(\nabla\phi^h - \boldsymbol{P}^r_{\Delta_K}\left(\nabla\phi^h\right)\right) \cdot \boldsymbol{w} d\boldsymbol{x} = 0 \quad \forall \boldsymbol{w} \in \left[\mathbb{P}_r\left(\Delta_K\right)\right]^2,$$

where $\left[\mathbb{P}_r\left(\Delta_K\right)\right]^2 = \left\{x_1^i x_2^j \mid i+j \leq r\right\}$ is the set of polynomials of degree r defined on patch Δ_K. For $r = 0$, the explicit formula for the recovered gradient is given by

$$\boldsymbol{P}^0_{\Delta_K}\left(\nabla\phi^h\right) = \frac{1}{|\Delta_K|} \sum_{T\in\Delta_K} |T| \nabla\phi^h \Big|_T$$

this is an area-weighted average of the discrete gradient over the patch Δ_K. The process is schematically represented in figure 7.1. From now on, whenever the polynomial degree r is not explicitly stated in the notation, it is assumed to be $r = 0$.

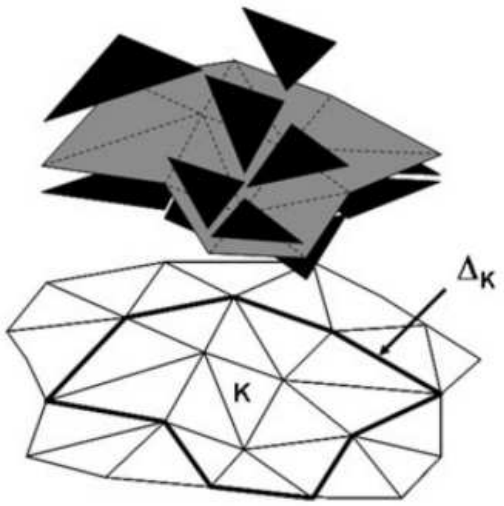

Figure 7.1: Schematics of the gradient reconstruction, image credits [54]

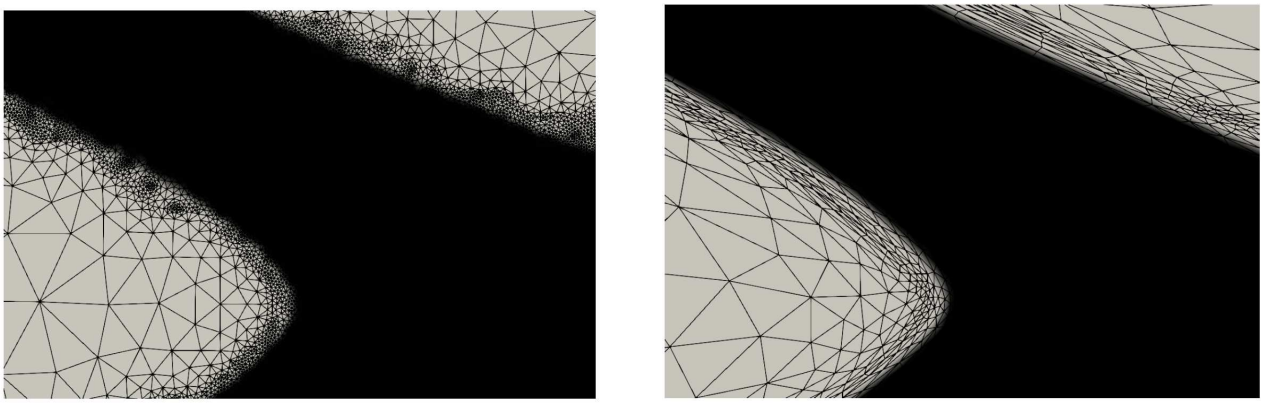

Figure 7.2: Isotropic vs anisotropic mesh adaptation, image credits [45]

The key component needed to extend this framework to anisotropic element is the invertible affine function $T_K : \widehat{K} \to K$, mapping the reference element inscribed in the unitary circle centered at the origin to any element on the mesh. The information regarding this transformation is encoded in the Jacobian matrix, identified by the symbol M_K. A polar decomposition yields

$$\mathrm{M}_K = \mathbf{B}_K \mathbf{Z}_K$$

with $\mathbf{B}_K$ symmetric positive definite and $\mathbf{Z}_K$ orthogonal matrix.
$\mathbf{B}_K$ can be further factorized into

$$\mathbf{B}_K = \mathbf{R}_K^T \mathbf{\Lambda}_K \mathbf{R}_K$$

via a spectral decomposition. $\mathbf{R}_K^T = [\boldsymbol{r}_{1,K}, \boldsymbol{r}_{2,K}]$ is the matrix containing the right eigenvectors of $\mathbf{B}_K$ and $\mathbf{\Lambda}_K = \mathrm{diag}\,(\lambda_{1,K}, \lambda_{2,K})$ is the diagonal matrix collecting the corresponding eigenvalues, with $\lambda_{1,K} \geq \lambda_{2,K} > 0$. It is also useful to define the so-called stretching factor $s_K = \lambda_{1,K}/\lambda_{2,K} \geq 1$.
The anisotropic global error estimator is given by the sum of all the local estimators as

$$\eta^2 = \sum_{K \in \mathcal{T}_h} \eta_K^2$$

The element-by-element contributions are defined as

$$\eta_K^2 = \frac{1}{\lambda_{1,K}\lambda_{2,K}} \sum_{i=1}^{2} \lambda_{i,K}^2 \left(\boldsymbol{r}_{i,K}^T \mathrm{G}_{\Delta_K} \boldsymbol{r}_{i,K} \right)$$

with $\mathrm{G}_{\Delta_K} \in \mathbb{R}^{2\times 2}$ symmetric positive semi-definite matrix with entries

$$[\mathbf{G}_{\Delta_K}]_{ij} = \sum_{T \in \Delta_K} \int_T \left[\boldsymbol{P}_{\Delta_K} \phi^h - \nabla \phi^h \Big|_{\Delta_K} \right]_i \left[\boldsymbol{P}_{\Delta_K} \phi^h - \nabla \phi^h \Big|_{\Delta_K} \right]_j d\boldsymbol{x}.$$

It is now possible to use the local estimator η_K to generate the metric $\mathcal{M}$. In practice, $\mathcal{M}$ is approximated with a piecewise constant function $\mathcal{M}|_K$ related to the mesh $\mathcal{T}_h$ by the equation

$$\mathcal{M}|_K = \mathbf{R}_K^T \Lambda_K^{-2} \mathbf{R}_K \quad \forall K \in \mathcal{T}_h$$

This requires solving the minimization problem for the local estimator

$$\begin{array}{ll} \min & \mathcal{J}_K\left(s_K, \boldsymbol{r}_{1,K}, \boldsymbol{r}_{2,K}\right) = s_K \boldsymbol{r}_{1,K}^T \widehat{\mathrm{G}}_{\Delta_K} \boldsymbol{r}_{1,K} + s_K^{-1} \boldsymbol{r}_{2,K}^T \widehat{\mathrm{G}}_{\Delta_K} \boldsymbol{r}_{2,K} \\ \text{s.t.} & s_K \geq 1, \\ & \boldsymbol{r}_{i,K} \cdot \boldsymbol{r}_{j,K} = \delta_{ij} \end{array}$$

The solution of this problem is given when $s_K = s_K^\star$ and $\boldsymbol{r}_{i,K} = \boldsymbol{r}_{i,K}^\star$, with

$$\begin{aligned} s_K^\star &= \sqrt{\frac{\theta_1}{\theta_2}}, \\ r_{1,K}^\star &= t_2, \quad r_{2,K}^\star = t_1, \end{aligned}$$

where $\{\theta_i, \boldsymbol{t}_i\}_{i=1,2}$ are the eigen-pairs associated to $\widehat{\mathbf{G}}_{\Delta_K}$ with $\theta_1 \geq \theta_2 > 0$ and $\{\boldsymbol{t}_i\}_{i=1,2}$ orthonormal.
The last piece is obtained combining previous equations into

$$\begin{aligned} \lambda_{1,K}^\star &= \theta_2^{-1/2} \left(\frac{\tau^2 \left\| \nabla \phi_h \right\|_{\Delta_K}^2}{2|\widehat{K}|} \right)^{1/2}, \\ \lambda_{2,K}^\star &= \theta_1^{-1/2} \left(\frac{\tau^2 \left\| \nabla \phi_h \right\|_{\Delta_K}^2}{2|\widehat{K}|} \right)^{1/2}. \end{aligned}$$

where $\widehat{K} = T_K^{-1}(K)$ is the pullback of the element K, τ is a tolerance parameter and

$$\left\| \nabla \phi_h \right\|_{\Delta_K}^2 = \frac{1}{|\Delta_K|} \sum_{T \in \Delta_K} |T| \left\| \nabla \phi_h|_T \right\|^2.$$

Therefore, given the eigenpairs $\left\{\lambda_{i,K}^\star, \boldsymbol{r}_{i,K}^\star\right\}_{i=1,2}$ it is possible to compute the optimal metric $\mathcal{M}^\star$ for all elements $K \in \mathcal{T}_h$. Finally, a relaxation technique is employed to avoid big discontinuities in the size of the elements. That is, calling $\mathcal{M}_\nu^\star$ the final metric and $\mathcal{M}_{\mathrm{OLD}}$ the old one,

$$\mathcal{M}_\nu^\star = \nu \mathcal{M}^\star + (1-\nu) \mathcal{M}_{\mathrm{OLD}}, \quad \nu \in [0,1]$$

Chapter 8

Acknowledgments

Il primo ringraziamento va a Camilla che in questi due anni mi ha dato la forza di superare i momenti difficili, anche quanto centiania di kilometri di distanza ci separavano. Grazie Cami, per ricordarmi perché il mio impegno ne vale la pena. Un ringraziamento alla mia fantastica famiglia, senza il vostro supporto non avrei potuto fare niente di tutto ciò, né Padova, né tantomeno Barcellona. A mio padre che mi ha sempre consigliato, a mia madre che mi ha sempre sostenuto, e ai miei fratelli Sara e Francesco che ho sempre sentito vicini, anche da lontano. Senza mamma non avrei mai cercato progetti internazionali e nessuno avrebbe saputo di questo progetto, quindi anche Giorgio ti è molto grato. Grazie ai nonni, che mi fanno sempre sentire molto amato. Grazie a Giorgio, con cui ho condiviso questo ultimo anno e mezzo con gioie e dolori, ma soprattutto tanti, tanti insulti ad alcuni corsi. Un grazie anche a tutti gli amici di Padova, ogni volta che sono tornato mi hanno fatto sentire come se non fosse passato un giorno per l'affetto con cui mi hanno accolto. Un grazie a tutti gli amici di Palermo per cui non importa quanto tempo passi l'amicizia aumenta soltanto. Un ringraziamento particolare a Rick che (da Padova) ha condiviso con me tante ore di svago online. Un ringraziamento va a Rosa, Toni e Oscar, che sono stati e sono dei punti di riferimento in terra straniera. Un ringraziamento speciale va amche ai Professori Mario Putti e Antonia Larese, che sin dal loro esame mi hanno fatto innamorare di questa materia, e anche mentre mi trovavo all'estero non hanno mai mancato di fare sentire il loro supporto sia morale che molto pratico. Ultimo ma non per importanza voglio ringraziare il Prof. Matteo Giacomini, che mi ha fatto sentire apprezzato a livello accademico/professionale come mai prima dell'anno scorso, credendo in me anche in momenti in cui io stesso non vi credevo.